ISSN 1063-7761, Journal of Experimental and Theoretical Physics, 2019, Vol. 129, No. 4, pp. 757–782. © Pleiades Publishing, Inc., 2019.
Russian Text © The Author(s), 2019, published in Zhurnal Eksperimental'noi i Teoreticheskoi Fiziki, 2019, Vol. 156, No. 4, pp. 806–836.

Contribution for the JETP special issue in honor of I. M. Khalatnikov's 100th anniversary

High-Energy-Density Physics and Laser Technologies

S. I. Anisimov[a], **V. V. Zhakhovsky**[b], **N. A. Inogamov**[a,b,*], **K. P. Migdal**[b],
Yu. V. Petrov[a,c], **and V. A. Khokhlov**[a,**]
[a]*Landau Institute for Theoretical Physics, Russian Academy of Sciences, Chernogolovka, Moscow oblast, 142432 Russia*
[b]*Dukhov All-Russia Research Institute of Automatics, ul. Sushchevskaya 22, Moscow, 127055 Russia*
[c]*Moscow Institute of Physics and Technology (National Research University),*
Institutskii per. 9, Dolgoprudnyi, Moscow oblast, 141701 Russia
** e-mail: nailinogamov@gmail.com*
*** e-mail: khokhlov@itp.ac.ru*

Received May 30, 2019; revised June 11, 2019; accepted June 14, 2019

Abstract—This paper is devoted to the jubilee of I.M. Khalatnikov, the founder and the first director of the Landau Institute for Theoretical Physics of the Russian Academy of Sciences. I.M. Khalatnikov organized a first-class institute the studies at which cover a broad spectrum of research directions. The plasma and lasers department of the Institute conducts research on plasma physics problems, laser–matter interaction, questions pertaining to laser applications, and hydrodynamics problems. Much attention is given to solid-state physics with an emphasis on the behavior of matter in extreme conditions under intense laser irradiation. A number of new results are presented: the behavior of metals in two-temperature states (when the temperature of the electron subsystem of a metal is much greater than the temperature of the ion subsystem due to ultrafast laser heating); determining the boundaries of existence of a single-wave propagation mode of elastoplastic shock waves in ductile metal crystals; the formation of a laser torch from target materials and liquids under metal laser ablation of a metal into the surrounding liquid; the physical–mechanical consequences (melting, capillarity, recrystallization) of nonuniform (along the irradiated surface) energy dissipation caused by the interference of plasmon–polariton and laser electromagnetic fields.

DOI: 10.1134/S1063776119100169

1. INTRODUCTION

The works of the plasma and lasers department of the Landau Institute for Theoretical Physics of the Russian Academy of Sciences are mostly concerned with problems of high-energy-density physics. This is how the field of science in which materials of solid-state densities heated to temperatures of the order of an electronvolt is called. We are interested in pressures from intermediate to high ones (tens and hundreds of GPa) and tensile stresses up to 1–10 GPa causing the destruction of condensed phases. This is a difficult field whose study is needed for many important applications (planetary interiors, beam impacts, high-speed collisions of condensed bodies). The difficulties of describing the states referring to high-energy-density physics stem from the fact that the potential energy U of interatomic interactions is of the order of the kinetic energy K. Consequently, neither the theory of condensed solid and liquid phases, $K \ll U$, nor the theory of gaseous plasmas, $U \ll K$, is applicable.

In the applications under consideration (for example, beam impacts) we cannot restrict ourselves only to the thermodynamics of states with a high energy density. The systems are in motion and, therefore, the thermodynamic phenomena are intertwined with the hydrodynamic ones. The motions can be both slow (we then apply equilibrium thermodynamics) and superfast. We apply kinetic approaches to describe superfast changes. In kinetics additional equations with additional time derivatives are added to the system of hydrodynamic equations with the time derivatives of the density, velocity, and internal energy on their left-hand sides. For example, an additional energy equation appears in the case of the high-energy-density physics of a two-temperature medium. This is discussed below in the text of the paper.

The processes initiated by laser beams lead to material compressions and extensions. Therefore, in this paper we consider the physics of shock waves and phenomena taking place under volume expansion. The expansion of hot condensed media is accompanied with evaporation. In turn, the vapors cool down and condense as the density decreases (nanoparticle production). This process is particularly complex when the vapors expand into the surrounding liquid (laser ablation into a liquid medium).

The extension of less hot ($U > K$) materials by inertia at a sufficient amplitude of the extension rate gradient leads to mechanical destruction of the condensed phase. One talks about the fragmentation or spallation in a continuous medium. For the solid phase the fragmentation is connected with the formation of a network of cracks [1]. In a melt the nucleation of bubbles, cavitation, occurs. The volume occupied by the bubbles in a liquid–vapor mixture increases under negative pressure. This is how the foamed layers are formed, whose evolution has an effect on the composition of the escaped particles and on the surface structures remaining after the impact.

Under laser action on films, the phenomena of cavitation on the frontal side of the film and spallation in the solid medium on the rear side of the film can combine in a surprising way [2]; the irradiated surface is called the frontal one. Moreover, the evaporation of outer layers combines with the cavitation and foaming of deeper layers on the frontal side at sufficient energetics.

The effects due to phase transitions play an important role. Melting has a very significant effect. The transition to the liquid phase abruptly removes the resistance to body shape deformation. The dynamics changes qualitatively; the extension of films and the transfers of matter to considerable distances begin.

The reverse transition from the liquid to solid phase manifests itself equally remarkably, especially when the crystallization zone propagates through a moving body. A wide variety of surface structures, from solitary ones like cupolas under sharply focused laser irradiation (small spot) to complex solidified surfaces, are formed precisely in this way. Such surfaces appear after ultrashort laser irradiation (up to a few picoseconds in duration) and at a large spot area (with an irradiation spot size from tens of micrometers).

The perturbations within large spots are a pile-up of frozen membrane walls surrounding concave pits and solidified jets often with a droplet above at the jet apex. Debris in the form of spheres lies on the surface. These are the droplets detached and returned back by surface tension. The pits are the traces of foam bubbles. Complex structures are formed under both optical and X-ray irradiation due to the competition of inertia, capillary forces, and fast recrystallization: cooling at a rate of 10^{12} K s^{-1}, melt supercooling of hundreds of degrees, and limiting propagation speeds of freezing zones ~100 m s^{-1} (they are determined by the diffusion of atoms in the melt). Consequently, plasmons have little effect on their formation (the X-ray frequencies are much greater than the plasma ones).

Much attention in the literature is given to the production of nanoparticles. Laser ablation into a liquid is an ecologically clean variant of such production. Today the theory of the corresponding processes lags significantly behind the experiment, where, acting empirically, practitioners apply a wide variety of irradiation conditions in duration, energetics, and impact spot size. Below in the paper we consider the problem of the description of ablation under irradiation through the transparent liquid of a light-absorbing target.

The technological direction using combined impacts belongs to the advanced ones. The electromagnetic waves from a laser and surface plasmon polaritons add up. Fine control of the spatial dissipation power distribution in the skin layer of a metal is exercised in this way on microscales. Perfect synchronization in time and space, coherence, and phase characteristics of waves are used. The power distribution is related to interference and the formation of a standing wave. As a result, a hologram (a specified relief on the surface) is recorded, with a plasmon polariton with a specified phase being initiated on the surface under its illumination [3].

The activity of the department of the Landau Institute for Theoretical Physics of the Russian Academy of Sciences is connected with the construction of physical models and predictive numerical simulations on this basis. In many respects, such simulations is based on the equations of thermodynamic state for pertinent materials. The present-day equation-of-state database was created at the Joint Institute for High Temperatures of the Russian Academy of Sciences and the Institute for Problems of Chemical Physics of the Russian Academy of Sciences [4–7]. The impetus to the development of a computational–experimental equation-of-state database associated with the Vega mission, the Venus and Halley's Comet project (see the next section), was important. Physical models are needed to theoretically describe and optimize the laser experiments that are being carried out at M.B. Agranat's department of the Joint Institute for High Temperatures of the Russian Academy of Sciences.

The paper is structured as follows. The questions related to the equations of state for condensed matter and their hydrodynamic applications are outlined in Section 2. Section 3 is devoted to the physics of the interaction of ultrashort laser pulses with matter. The results on shock waves in solids are presented in Section 4. The problems of an ultrahigh-speed impact are outlined in Section 5. Sections 6 and 7 are devoted to astrophysical applications and laser technologies, respectively.

In the 1960s–1990s many fundamental results were obtained in the department under the leadership of S.I. Anisimov. They refer to a plasma corona and laser thermonuclear fusion [8, 9], conical targets for the generation of neutrons under laser action [10]; the Vlasov equations, plasma parametric instabilities, and

Langmuir collapse [11–13]. The evaporative ablation [14–17] and the ablation front instability [17–19] were studied in detail. The stability of the melting and recrystallization fronts was analyzed [18–23]. The hydrodynamic and Knudsen regimes of vapor expansion and the coexistence of these regimes were studied [24–28]. The evaporation kinetics is a complex, multistep process [28]. The three-dimensional effects of the expansion [29, 30] and compression of a spherical target [31] were described using an elegant exact solution (ellipsoids with a linear velocity distribution along the radius). This approach originates from the well-known classical solutions for rotating bodies like a Maclaurin spheroid and Dirichlet ellipsoids; during rotation the velocity distribution is a linear function of radius. An additional integral of motion is used in the solution. Recently, E.A. Kuznetsov has found out that the mathematically corresponding equations are coupled with Ermakov's systems [32]. It was discovered that the optical dielectric breakdown is associated with submicron inclusions [33–37]. The works on electron photoemission, metallic hydrogen, and liquid crystals are important. A huge work was done on hydrodynamics and hydrodynamic instabilities. Unfortunately, an overview of all these studies is too large and goes far beyond the scope of this paper devoted to new results.

2. EQUATIONS OF STATE AND A HIGH-VELOCITY IMPACT

Vega turned out to be the most successful of all Soviet space research projects. This is because of, first, the competent management of the institutes and the concerted actions of various subdivisions of the Academy of Sciences of the USSR and, second, the fruitful work of scientists. The Landau Institute for Theoretical Physics in the person of its director I.M. Khalatnikov made a substantial contribution to the project (awarded the State Prize of the USSR). The time-proven tandem of S.I. Anisimov's department and the research team of the Institute for High Temperatures headed by V.E. Fortov worked effectively.

As a result, two very important goals were achieved.

(1) An original concept of spacecraft dust protection was proposed, justified, and implemented [38–41]. The protection was accomplished in the form of a bumper shield with two sheets, with the first sheet acting as a vaporizer of superfast cometary dust grains.

(2) The Photon instrument was constructed and installed onboard the spacecraft. Data on the coarsest cometary dust fraction in the comet coma were obtained for the first time with this instrument [42].

A fleet of six satellites created and controlled by four national space agencies was sent to the comet. Two Russian spacecraft, Vega 1 and Vega 2, and Giotto—a creation of the European Space Agency, were the most important component of the fleet. These three spacecraft were equipped with a lot of scientific instruments. Many of them were designed at the Space Research Institute; the principal investigator of the project was R.Z. Sagdeev. Vega 1 and Vega 2 played a key role. The point is that the Giotto spacecraft flying behind Vegas was accurately pointed toward the comet owing to the detailed information about the comet trajectory arrived from them. The rendezvous of Vegas with the comet at distances of 9000 and 8000 km occurred on March 6 and 9, 1986.

Several days after the flight correction using the Soviet spacecraft (on the night from March 13 to 14, 1986), Giotto flew at a distance of 600 km from the comet nucleus. Being so close to the nucleus in the period of perihelion passage by the comet, Giotto was significantly damaged. Halley's Comet passed through the perihelion of its orbit on March 10. On the days of perihelion passage the activity of the comet was highest due to its proximity to the Sun.

Very valuable information about the comet was obtained; the preliminary reports alone filled the May issue of Nature (vol. 321, May 15, 1986). There are several thousand references to them. For example, the sizes of the comet, a giant structure with a volume of the order of the annual drainage of Volga or of the order of the Elbrus Vulcan, were accurately determined. The comet turned out to reflect the light very poorly (its albedo is a few percent, blacker than coal, the so-called "March snow") and to be strongly heated. The dust composition was studied—there is much organics (important for the concepts of the origin of life on Earth); the grain size distribution at various distances from the comet was determined. The above-mentioned Photon instrument provided data on large dust grains and recorded a strong spatial inhomogeneity of the dust cloud [42].

Vegas flew to the comet for more than one year; the coma passage at distances of ~10000 km took about 5 min. This was because the velocity with which the spacecraft approached the comet nucleus was extremely high (80 km s^{-1}!) (the proximity to the Sun and the rendezvous head-on). The central zone of the coma at the stage of perihelion passage was filled with dense gases and high-concentration cometary dust. That is why the above-mentioned problem of spacecraft dust protection was extremely important.

Of course, studies at velocities of ~100 km s^{-1} are not a problem where individual atoms are involved. However, here we are talking about condensed particles with a mass up to 10^{-9} g and sizes up to 10 μm. So far there are no devices on Earth in which particles of such a mass could be accelerated to 100 km s^{-1}. Only submicron-sized particles are accelerated to this velocity on a Van de Graaff (electrostatic) accelerator at a limiting voltage of 2 MV, which the mass control being a separate problem.

Huge work was carried out over several years to prepare the flight. The work was carried out at the Landau Institute for Theoretical Physics of the Academy of Sciences of the USSR (the director I.M. Khalatnikov) in S.I. Anisimov's department in collaboration with V.E. Fortov's research team. If necessary, specialists of other subdivisions were invited to participate: the Lavochkin Research and Production Association, the Moscow Aviation Institute, the Institute of Solid State Physics, and the Space Research Institute. As a result, before the flight it was clear how an ultrafast cometary dust grain interacted with the spacecraft structures.

How can this be clarified without a direct experiment? Powerful codes for three-dimensional collision computations were developed. The equations of state for condensed matter were carefully described. The most important contribution of V.E. Fortov's team was the development of multiphase wide-range equations of state [39, 40].

The point is that a huge kinetic energy, about half a million degrees pen nucleon, is dissipated in such an interaction; for comparison, the energy per nucleon under the impact of an armor-piercing shell is lower by four orders of magnitude. Therefore, all phases, from a crystal to a melt and from a melt to evaporation and heating to the plasma state, should be encompassed. Let us explain the necessity of wide-range equations of state.

During the rendezvous with Halley's Comet the energy per atom, say, of iron is ~2 keV at the first ionization potential of 8 eV. Thus, a plasma of multiply charged ions emerges in the near impact zone, while the temperature drops by more than an order of magnitude (due to the expenditure on ionization) compared to the temperature of ~2 keV that would be when neglecting the ionization. Subsequently, the density and temperature decrease rapidly due to expansion; the impact products are a recombining plasma, a gas of neutrals, clusters of condensates, droplets of hydrodynamic liquid ejection, and solid particles of peripheral spallation destruction. The products fly apart in wide ranges of emission angles and velocities from tens of km s^{-1} to tens of m s^{-1}.

Before the flight comet scientists neglected the ionization in their estimates (a dust grain was represented by the equation of state for an ideal gas), while the shock wave in the barrier was described as a strong Sedov shock; recall that this solution is suitable only for an ideal gas with a fixed adiabatic index. Hence a huge role of hydrodynamic codes in real geometry and with real equations of state is clear. Such necessary studies were performed in S.I. Anisimov's department in collaboration with V.E. Fortov's team.

Moreover, the numerical studies were supplemented by comparisons with full-scale experiments, which allowed the adequacy of physical models and applied codes to be proven. The experiments were carried out with the application of lasers and high-current relativistic electron beams (Angara) [41]. The impact parameters (energetics, duration, spot size) corresponded to the impact of a cometary dust grain.

As a result of these works, a system of spacecraft protection against incoming cometary dust was designed. Thus, an invaluable contribution to the successful execution of the project was made.

3. ULTRASHORT PULSES

Our department may be called the founder of the theory of high-power ultrashort laser action. Indeed, the classic paper [43], where the physics of various phenomena arising under irradiation of matter by ultrashort pulses is described, was approximately ten years ahead of the creation of such lasers in the 1980s. The exceptional importance of this subject matter using femtosecond lasers was noted in 2018 by awarding the Nobel Prize for Physics (G. Mourou, A. Ashkin, D. Strickland) [43].

3.1. The Physics of Two-Temperature States

The two-temperature states are required to be taken into account in the cases where an ultrashort (with a duration $\tau_L \sim 0.01-1$ ps) laser pulse acts on a metal. The point is that the absorbed laser energy dissipates in the electron subsystem; in this case, the temperature equilibrium between the electron and ion subsystems has no time to be established in the pulse action time [43]. Accordingly, the electron temperature T_e turns out to be much higher than the ion temperature T_i. At present, the theory of two-temperature states started with the pioneering papers [43, 44] already has a long history of its development [45, 46]. In this section we describe the approaches and the results obtained in the department to the thermal physics (equation of state) and kinetic coefficients (thermal conductivity and electron–ion heat exchange coefficient) of materials in two-temperature states.

In addition to the parameter τ_L, which defines the laser action duration, there are three intrinsic relaxation time scales: $\tau_{ee} = 1/\nu_{ee}$, $\tau_{ei} = 1/\nu_{ei}$, and $\tau_{ii} = 1/\nu_{ii}$, defined by the electron–electron, electron–phonon, and phonon–phonon collision frequencies. The energy distributions of electrons and ions depend on them.

A Fermi distribution of electrons with a current local (in material) temperature $T_e(x, t)$ is established in times of the order of $\tau_{ee} = 1/\nu_{ee}$; for simplicity, we talk about the one-dimensional case with a spatial coordinate x. The frequency ν_{ee} increases approximately as the square of the electron temperature up to temperatures $T_e \sim 1$ eV [47]; at higher temperatures T_e the increase of the function $\nu(T_e)$ slows down sharply [47]. The estimates from [48, 49] show that if the energy absorbed in the time of an ultrashort pulse exceeds ~1 mJ cm^{-2}, then a Fermi distribution in the metal is established in a time of the order of the duration of the pulses considered here, 0.1 ps. We are interested in the situations where the energy absorbed by the target exceeds the melting and ablation thresholds. The typical ablation thresholds are ~100 mJ cm^{-2}; the melting threshold is several times lower. Therefore, it is admissible to use the temperature T_e to describe the electron subsystem from the earliest pulse action stages.

The electron–electron and electron–ion collision cross sections are comparable, but the time t_{eq} of absorbed energy transfer from the electron subsystem to the ion one is much greater than a time scale of the order of τ_{ee} due to the large ion-to-electron mass ratio; of course, this is said for our range of absorbed energies beginning from values of the order of tens and hundreds of mJ cm^{-2}, where τ_{ee} decreases to 1–10 fs. The isolation of the physics of two-temperature states into a separate research direction is explained by this fact. Let us explain that the free flight times in electron–electron (τ_{ee}) and electron–ion (τ_{ei}) collisions (under the conditions of interest to us) are comparable, while t_{eq} is much greater than τ_{ee} and τ_{ei}.

Here, it is appropriate to clarify the two-temperature model with regard to the phonon subsystem. The approximation of an isotropic elastic body and the Debye model of a solid body with longitudinal and transverse modes are usually applied; it is assumed that the temperatures of the phonon subsystem are higher than the Debye one and that the phonon subsystem is in equilibrium, i.e., characterized by the ion temperature T_i. In this case, the frequency of the hardest phonon modes is ~10 THz, i.e., their periods are ~100 fs. Clearly, the thermalization time of these modes (mode lifetime) exceeds the period at least by an order of magnitude, i.e., ~1 ps or more. A supersonic electron that generates a longitudinal phonon through the Cherenkov mechanism produces mostly the hardest longitudinal acoustic phonons if there are no optical modes. If such modes are present, then both optical and high-frequency acoustic phonons are generated.

Subsequently, the hard phonons decay due to the presence of anharmonic corrections. It takes a long time for the phonon temperature to be established. It takes a particularly long time for the equilibrium (in temperature) long-wavelength tail of the distribution (up to nanoseconds) to be formed [50–52]. However, the soft part of the phonon distribution contains a small fraction of the energy and, therefore, is insignificant in the energy balances. We see that the time it takes for a complete or effective equilibrium to be established in the phonon subsystem is comparable to the electron–electron relaxation time t_{eq} or exceeds this time.

A number of papers devoted to analyzing the influence of phonon distribution nonequilibrium on the electron–phonon relaxation rate have appeared [53–58]. According to [53], in aluminum the corresponding correction to the electron–phonon relaxation coefficient is of the order of tens of percent. On the other hand, the calculations in [56] give a few percent for this correction.

Thus, first, the separation of two-temperature studies into an independent branch of science is connected with the relative lifetime of the system in such states. Second, it turns out (see below) that the thermodynamic and kinetic characteristics of two-temperature materials differ significantly from those in one-temperature states. The electron contributions to the thermodynamics (the change of the equation of state) and the increase in electron thermal conductivity are most important for calculating the dynamics of targets with two-temperature relaxation in them. In this case, the relaxation duration is determined by the electron–ion energy exchange coefficient. The pressure of hot electrons stretching the ion subsystem plays an important role at the stage of incomplete electron–ion relaxation. Furthermore, the two-temperature thermal conductivity of metals can be much greater than the thermal conductivity at room temperature.

The system of two-temperature hydrodynamic equations in a one-dimensional geometry written in Lagrangian coordinates is [59]

$$\rho(x^0,t)\frac{\partial x(x^0,t)}{\partial x^0} = \rho^0, \tag{1}$$

$$\rho^0\frac{\partial u}{\partial t} = -\frac{\partial p(x^0,t)}{\partial x^0}, \tag{2}$$

$$\frac{\partial x(x^0,t)}{\partial t} = u(x^0,t), \tag{3}$$

$$\rho^0\frac{\partial(E_e/\rho)}{\partial t} = -\frac{\partial q}{\partial x^0} - \dot{E}_{ei} + \frac{\rho^0}{\rho}Q - p_e\frac{\partial u}{\partial x^0}, \tag{4}$$

$$\dot{E}_{ei} = \frac{\rho^0}{\rho}\alpha(T_e - T_i), \qquad q = -\frac{\rho\kappa}{\rho^0}\frac{\partial T_e}{\partial x^0}, \tag{5}$$

$$\rho^0\frac{\partial(E_i/\rho)}{\partial t} = \dot{E}_{ei} - p_i\frac{\partial u}{\partial x^0}, \tag{6}$$

$$Q = \frac{F_{abs}}{\sqrt{\pi}\tau_L\delta}\exp\left(-\frac{t^2}{\tau_L^2}\right)\exp\left(-\frac{x}{\delta}\right)\theta(x). \tag{7}$$

Above we have written the mass conservation law (1), the trajectory $x(x^0, t)$ of a material particle with a Lagrangian coordinate x^0, $x(x^0, t = -\infty)$, ρ^0 is the initial density. The momentum conservation law is represented by Eq. (2), where $u(x^0, t)$ is the Lagrangian particle velocity. The kinematic condition has the form (3). The energy conservation law is written separately for the electron and ion subsystems. The energy balance in the electron subsystem is given by Eq. (4) [43]. The power of the energy exchange between the electron and ion subsystems per unit volume and the electron heat flux are given by Eqs. (5). The energy bal-

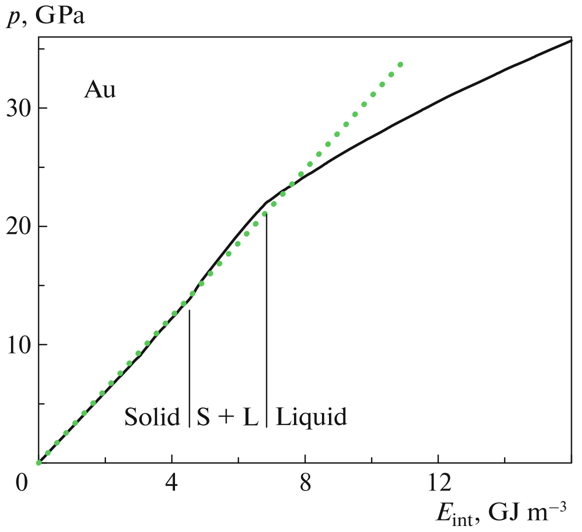

Fig. 1. (Color online) The gold isochore constructed according to the wide-range equation of state (solid curve) [5–7, 66, 71, 72] and in accordance with the Mie–Grüneisen approach (green dots). In the latter case, the Grüneisen parameter does not depend on temperature and is 3.1 for the specified density that on this isochore is equal to the density under normal conditions, 19.3 g cm^{-3}. The behavior on the isochore is important, because when irradiated by an ultrashort pulse with an absorbed energy of the order of or higher than the ablation threshold, a ~100-nm-thick layer melts in a time t_m of the order of a few picoseconds. The rarefaction wave traveling away from the boundary with a vacuum has time to traverse a distance $c_s t_m$ ~ 5–10 nm. Therefore, the density of the material in the heating layer changes little. There are three regions referring to the solid phase, the liquid–crystal mixture, and the melt.

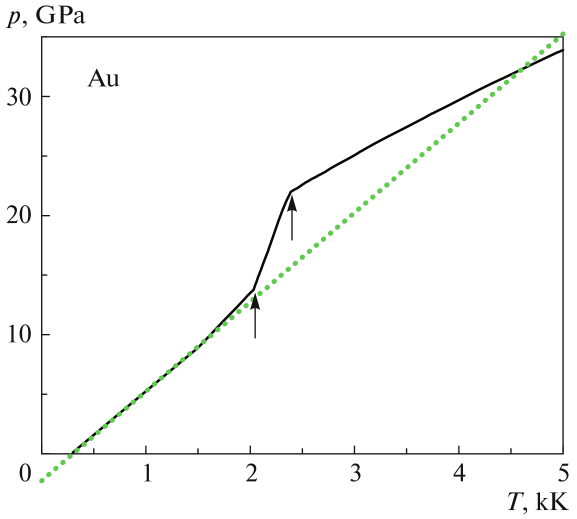

Fig. 2. (Color online) The gold isochore (cf. Fig. 1). In these variables the Mie–Grüneisen isochore (green dots) and the isochore from the wide-range equation of state (solid curve) differ more dramatically. The arrows mark the intersection of the solidus and liquidus with the isochore. In the melting region the pressure on the isochore rises much faster than it does in the single-phase regions.

ance in the ion subsystem is described by Eq. (6). The heating power per unit volume due to the absorption of laser radiation pulse is specified by Eq. (7), where δ is the skin layer thickness and τ_L is the laser pulse duration. Formula (7) with the function $\theta(x)$, $x > 0$, and $\theta(x) = 0$, $x < 0$, is valid for moderate-intensity ultrashort pulses, when the shift of the contact boundary in the pulse action time may be neglected. At the initial time it is at the point $x = 0$. The absorbing material is located on the right, at $x > 0$.

The system of two-temperature equations (1)–(7) represents the mass, momentum, and energy conservation laws. We provided this system here to pinpoint the places in which the terms representing the equation of state, the thermal conductivity, and the electron–ion heat exchange coefficient appear in the equations. The total pressure $p = p_e + p_i$ enters into Eq. (2) for the momentum. The thermal conductivity κ removes (4), (5) the heat absorbed by electrons from the skin layer. Heat is transferred from electron to electron into the target along the electron subsystem. Concurrently, there is heat transfer from hot electrons to cold ions at all distances from the target boundary.

Thus, the equation of state, the thermal conductivity, and the heat exchange coefficient α (5) should be known to solve the system. The equation of state relates the internal energy, the pressure, and the temperatures of the subsystems T_e and T_i.

3.2. The Equation of State

The equations derived in our department describe the two-temperature ($T_e \gg T_i$) and one-temperature ($T_e \approx T_i$) states in a unified continuous way [60–62]. The electron contribution dominates at high temperatures T_e: the electron thermal pressure exceeds the ion thermal pressure and the electron thermal conductivity begins to exceed $3k_{\rm B}$ (Dulong–Petit law), where $k_{\rm B}$ is the Boltzmann constant. At $T_e \approx 2$ eV the condensed phase for different metals and, accordingly, the bound state of matter cease to exist even at low temperatures T_i of the phonon subsystem (see Figs. 2b and 2c in [63]). Thus, this temperature is an analogue of the critical temperature in the one-temperature case. When heated to $T_e \approx 2$ eV for a cold ion subsystem and a low external pressure, the metal expands by tens of percent before the bound states cease to exist. In this case, the electron pressure begins to exceed the maximal voltage across the resistance that the condensed matter can produce in response to its stretching. This emphasizes the importance of research on the physics of two-temperature states.

The idea of analytical approximations of the descriptions of two-temperature states is to separate the electron (F_e) and ion (F_i) contributions to the free energy:

$$F = F_e + F_i. \tag{8}$$

Accordingly, the contributions to the pressure $p = p_e + p_i$ and the internal energy $E = E_e + E_i$ are broken down into the same sum. The separation (8) was proposed in the 1960s in various works on constructing the equations of state for condensed matter at high temperatures [4, 40, 64–67] (see also [5–7, 68–70]). We are talking about condensed states, i.e., states with a high density of matter. In our situations we can talk about the physics of two-temperature states with a high energy density—two-temperature warm dense matter. We emphasize that in early works these were one-temperature equations of state, i.e., the electron and ion temperatures were equal.

At temperatures of the order of the temperature at the critical point and densities of the order of the density of matter at the critical point, the electron contribution in metals is comparable to the ion contribution (here this is discussed as applied to one-temperature states). In this case, the ion contribution to the pressure is negative, while the electron one is positive. Their difference forms a critical pressure p_c noticeably lower than the absolute values of the terms of each contribution.

In the approximation (8) only the thermal contribution p_e is associated with the electrons. In this sense, the two-temperature equation of state is similar to the equation of state in the Mie–Grüneisen approximation:

$$p = p_{\text{cold}}|_i + p_T|_i + p_e. \tag{9}$$

The thermal contribution in the one-temperature case is p_T. In the two-temperature case (9) the thermal contribution breaks up into two contributions: the electron p_e with temperature T_e and the ion $p_T|_i$ with temperature T_i [45, 60].

Our approach to the two-temperature equation of thermodynamic state is as follows. The ion part F_i (8) either is taken from the multiphase wide-range equation of state [5–7, 66] or is approximated in the Mie–Grüneisen approximation. These approaches are compared in Figs. 1 and 2. The Solid and Liquid regions in Fig. 1 are separated by the S + L melting corridor, in which the two-phase mixture is located. According to Fig. 1, the increase in internal energy E_{int} under isochoric melting is 2.3×10^9 J m^{-3}. This quantity is equal to 23.6 kJ/mol per unit mass. The latent heat of melting for gold is considerably smaller, 12.55 kJ/mol. The minimum ion internal energy in a pure melt at a density of 19.3 g cm^{-3} is 6.85 GPa, or 0.27 eV/atom = 70 kJ/mol.

A shortcoming of the Mie–Grüneisen approximation compared to the multiphase equation of state [5–7, 66, 71, 72] is the absence of a saturated vapor pressure and a melting curve. From Figs. 1 and 2 it can be understood how significantly the absence of a latent heat of melting affects the results. The isochoric dependences are shown, because under ultrashort heating the volume expansion of matter at the two-temperature stage is small. We see from the dependences $p(E_{\text{int}})$ of pressure on internal energy that the difference is small if we restrict ourselves to the energy range shown in Fig. 1 and, accordingly, to the temperatures below 5 kK (cf. Figs. 1 and 2), with the melting heat having little effect on the dependences $p(E_{\text{int}})$. The decrease in the Grüneisen parameter in the liquid phase compared to the solid turns out to be more significant. In the Mie–Grüneisen model the Grüneisen parameter is determined from the solid phase and does not depend on temperature.

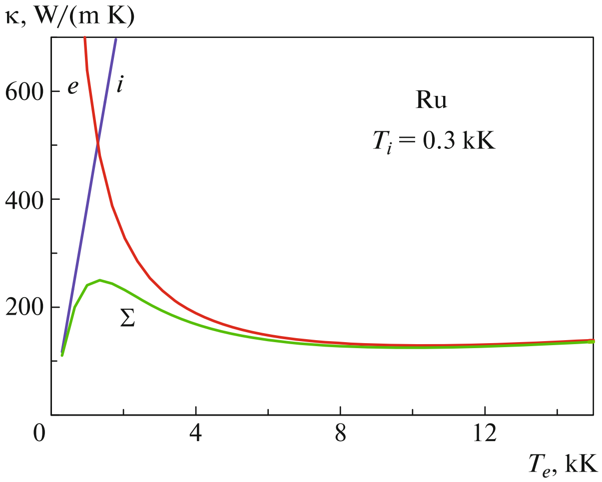

Fig. 3. (Color online) The thermal conductivity of solid ruthenium with a normal density of 12.45 g cm^{-3} in two-temperature states (curve Σ). The thermal conductivity Σ was obtained by adding the thermal resistances. These are partial resistances. One of them is related to the scattering of electrons carrying the heat flow by ions. The conductivity *i* corresponds to it. The second resistance is a consequence of the scattering of *s* electrons by ruthenium *s* and *d* electrons. It is represented by the conductivity *e*.

The difference in temperature between the two approaches is greater. This difference is concentrated in the melting region and reaches its maximum at the melting end point (the transition from a mixture to a pure melt). The melting start and end points are marked by the arrows in Fig. 2. The melting start temperature of 2030 K on the chosen isochore is higher that the gold melting temperature of 1337 K at low pressures. At the melting end point of 2390 K the Mie–Grüneisen pressure is lower by 6.4 GPa at equal temperatures, lower than the pressure from the multiphase equation of state. The Mie–Grüneisen temperature is higher by 860 K at equal pressures of 22 GPa.

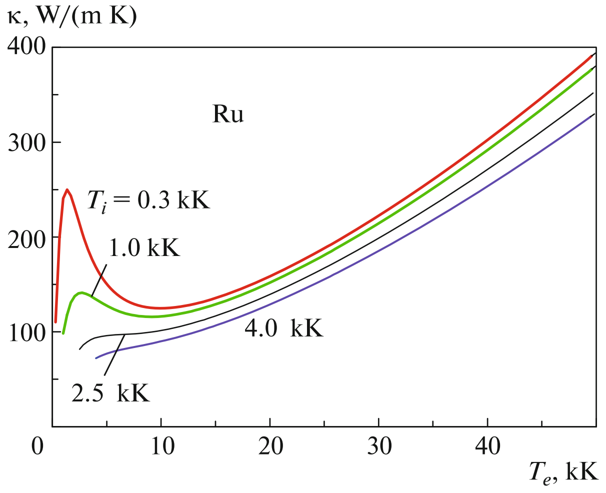

Fig. 4. (Color online). The thermal conductivity of solid ruthenium with a normal density of 12.45 g cm^{-3} in two-temperature states. It is shown how a rise in the temperature T_i of the ion subsystem affects the thermal conductivity. Above $T_e = 10$ kK a rise in T_i from 300 K by an order of magnitude is seen to change little thermal conductivity κ. This is because in this hot (in T_e) region the electron–electron scattering is the main one.

The influence of the replacement of the multiphase equation of state by the Mie–Grüneisen equation is analyzed in detail in [73]. The analysis was performed using a hydrodynamic flow in which a plate is perforated by a sphere flying at a high velocity as an example (see also Section 2 above). The shock adiabats of these approaches are virtually identical (see Fig. 4b in [73]). A huge difference between the approaches is seen in the unloading adiabats going from the states at high pressures behind the shock (several Mbar or higher). The difference in unloading adiabats arises and grows as the binodal (vapor–liquid phase equilibrium curve) is approached from high pressures. Clearly, since the evaporation is disregarded in the Mie–Grüneisen equation, this difference is attributable to the low vapor density in the mixture.

The electron part of the two-temperature equation of state is obtained through quantum-mechanical calculations in the density functional approximation. In this case, the ion subsystem is considered at $T_i = 0$ (the ions are at rest at lattice sites). The lattice constant is varied to understand the influence of a change in density. A series of calculations with a rising electron temperature is made for various densities. The electrons are distributed in energy in accordance with the Fermi distribution and in accordance with the spectrum of electronic state densities for given density and temperature T_e.

3.3. The Hydrodynamic Phenomena Associated with the High Thermal Conductivity of Metals in Two-Temperature States

Laser action consists in heating a material. If the pulse is ultrashort, then the hydrodynamic phenomena (the generation of acoustic compression and rarefaction waves) propagating with the speed of sound lag behind the thermal effects, because there is a supersonic propagation of heat into the heating layer [70, 74–77]. Here it is necessary to separate the stages of the thermal effects. As is clear from what has been said above, there are two thermal stages. They refer to the two-temperature and one-temperature stages, respectively. It is the two-temperature stage that proceeds with a supersonic speed [76, 78, 79], i.e., at this stage the heat absorbed in the skin layer propagates into the target at speeds greater than the speed of sound.

The physical reasons why the heat propagation speed can be supersonic are simple. First, this is because the magnitude of the Fermi velocity $v_F \sim 10^8$ cm s^{-1} (the electrons move with this velocity) is great compared to the speed of sound $c_s = (3–7) \times 10^5$ cm s^{-1} [76]. Second, the moderate ratio of the heating layer thickness d_T at the two-temperature stage to the thickness l_e of the Knudsen layer in electron mean free path plays an important role [76].

Indeed, from the formula $x(t) = 2\sqrt{\chi t}$, where $\chi = (1/3)l_e v_F$ is the thermal diffusivity, it is easy to derive

$$\frac{\dot{x}(t)}{c_s} = \frac{2}{3}\frac{M_F l_e}{x(t)} = \frac{1}{\sqrt{3}} M_F \sqrt{\frac{\tau_e}{t}}, \qquad (10)$$

where $M_F = v_F/c_s \sim 100$ is the Mach number in Fermi velocity, $\tau_e = l_e/v_F$, l_e is the electron mean free path. Let the transition between the two- and one-temperature stages occur as the Mach number of the heat wave decreases to $M_{\rm eq} \sim 1$. According to (10), the thickness d_T of the heating layer created at the two-temperature stage is then

$$d_T = \frac{2}{3}\frac{M_F}{M_{\rm eq}} l_e = 130\,\text{nm}. \qquad (11)$$

The numerical estimate in (11) was made for typical parameters $M_F = 100$, $M_{\rm eq} = 1$, and $l_e = 2$ nm. The duration of the two-temperature stage, at which the heating layer d_T grows supersonically, is estimated to be

$$t_{\rm eq} = (M_F^2/3M_{\rm eq}^2)\tau_e = 6\ \text{ps}. \qquad (12)$$

In the estimate (12) we used the parameters given above. In this case, the mean free time $\tau_e = l_e/v_F$ is 2 fs.

The supersonic propagation of heat is responsible for the emission of acoustic disturbances [70, 74, 76, 80]. The emission occurs in the transonic heat propagation segment. In this segment, the rate of heat propagation into the bulk of the heated layer decreases

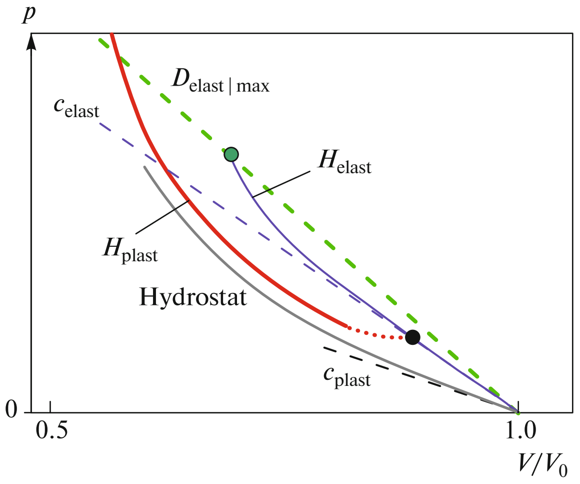

Fig. 5. (Color online) Hydrostatic compression (hydrostat curve) and shock adiabats, the elastic (H_{elast}) and plastic (H_{plast}) ones. The plastic (c_{plast}) and elastic (c_{elast}) speeds of sound are shown. The single-wave elastoplastic regime of propagation exists in the range between the limiting speed $D_{\text{elast}}|_{\max}$ of the single-wave structure and the elastic speed of sound c_{elast}.

from supersonic to highly subsonic. In the same segment the electron and ion temperatures are equalized and the two-temperature regime ends. If the penetration of heat into the volume is accompanied by a supersonic expansion of the melting layer in the material (in this case, the material is at rest, there is no geometrical expansion of the material), then a trace from the melting process remains on the rarefaction wave profile [70, 76]; the Grüneiser parameter is increased in the melting corridor between the solidus and liquidus; supersonic melting is called in the literature homogeneous melting; it is contrasted with slow (subsonic) heterogeneous melting in the spirit of Stefan's problem.

This trace is a steep compression wave segment (due to the increase in Grüneiser parameter in the melting corridor). The presence of such a segment accelerates the compression wave breaking and the shock formation and affects the shock splitting into an elastic precursor and a plastic shock [70, 76]. We will return to the problem of laser shock initiation below, in the section devoted to shock waves.

The hydrodynamic consequences of the sharp increase in thermal conductivity at the two-temperature stage were analyzed in our department [76, 79]. In Figs. 6 and 7 from [79] the mean expansion velocity of the melting layer is 20 km s^{-1}. The phenomenon of very fast heat propagation after the action of a femtosecond pulse at an early stage is seen on the graphs constructed numerically in many papers [81, 82]. Previously, however, this phenomenon was not associated with the two-temperature stage and with the sharp increase in thermal diffusivity at this stage. There were no physical explanations (Fermi velocity) why this diffusivity increases so dramatically either.

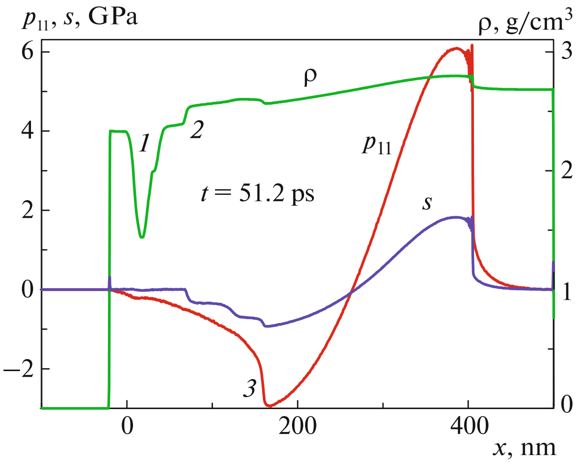

Fig. 6. (Color online) Profiles of the density ρ, longitudinal pressure p_{11}, and shear stress $s = (1/2)[p_{11} - (p_{22} + p_{33})/2]$. The shock amplitude is 6 GPa; *1* is the trace in the density profile from subsurface bubbles. The profiles are the results of averaging along directions 22 and 33 transverse to direction 11. Direction 11 is perpendicular to the initial position of the flat aluminum boundary. Mark *2* is the melting front, the liquid phase is to the left of this front; *3* is the spallation pulse that is formed at the time of bubble nucleation and removes the tensile stress. At the melting front the shear stress s abruptly becomes zero.

An exceptionally high speed of heat propagation from the skin layer into the film with a rapid attainment of the film rear side and heating of this side recorded in the experiment [83] was pointed out already in the first experimental works on the action of femtosecond pulses on thin films. Gold films 50–100 nm in thickness were used. The pump–probe

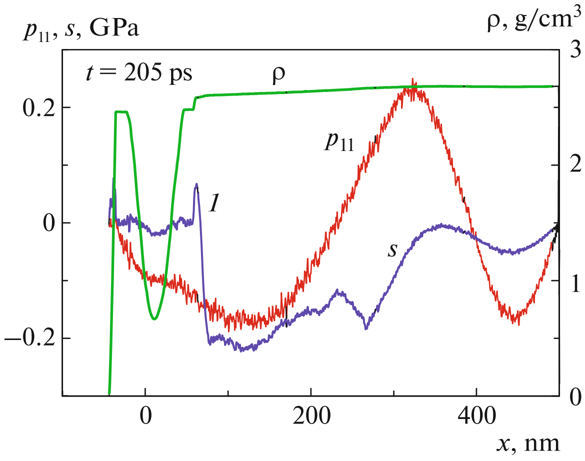

Fig. 7. (Color online) The profiles and designations are the same as those in Fig. 6. Note the change of sign of the stress s in the solid layer 1 near the molted layer.

technique for measuring the thermoreflectance, i.e., the change in reflectivity from the surface when heated, was applied.

At that time, experimenters explained such anomalously fast heat propagation by assuming the ballistic passage of electrons through the entire film thickness of ~100 nm without collisions. Actually, the electron mean free path is smaller. At the same time, however, the thermal diffusivity χ at the two-temperature stage is exceptionally large—it increases by two orders of magnitude compared to its values at room temperature.

Thus, an ultrashort pulse generates a number of thermal and hydrodynamic phenomena. If the target is thicker than the heating depth d_T, then the thermal evolution of the heating layer at the two-temperature stage is defined by two parameters, κ and α (see Eq. (5)). Given these parameters, the heating depth d_T and the relaxation duration $t_{\rm eq}$ can be estimated [59, 84].

In thin films ($d_f < d_T$) the material through the film thickness heats up rapidly, even before the end of two-temperature relaxation (d_f is the film thickness). The subsequent two-temperature thermal evolution depends on the parameter α. Note the interesting research on the hydrodynamics of thin films carried out in our department [63, 85–97]. The papers devoted to the hydrodynamics of thin films exposed to sharply focused (the illumination spot on the film is limited by the diffraction limit) ultrashort radiation pulses are listed here.

The recent paper [98] correlates with the above considerations regarding the sharp increase in thermal diffusivity at the two-temperature stage [97, 99]. The heating spot on the film has time to slightly expand radially in the two-temperature regime; it is of the order of d_T, but now d_T is the distance in the radial direction (and not along the normal to the film surface), small compared to the radius R_L of the laser heating spot if $R_L \approx 1$ μm or more. To record the effect, the radius R_L should be as small as possible (the diffraction limit and the application of lasers in the ultraviolet).

3.4. The Thermal Conductivity of Metals in Two-Temperature States

Beginning with the pioneering paper [43], much work has been done in our department to determine the thermal conductivity in the two-temperature regime [46, 47, 49, 61, 62, 75, 78, 100–109]. A proper description of the thermal conductivity is extremely important for two-temperature hydrodynamics simulations. After a short overview, we will present new results referring to such a refractory metal as ruthenium.

First the following formula was proposed [110, 111]:

$$\kappa = C\frac{(t_e^2+0.16)^{5/4}(t_e^2+0.44)t_e}{\sqrt{t_e^2+0.092}}\frac{1}{t_e^2+\beta t_i}, \qquad (13)$$

where $t_e = T_e/T_F$, $t_i = T_i/T_F$, T_F is the Fermi temperature. Formula (13) is based on the assumption that the electron–electron collision frequency increases as

$$\nu_{ee} = BT_e^2, \qquad (14)$$

where the coefficient B is constant if $T_e \ll T_F$.

The question is to what temperatures less than T_F does Eq. (14) hold? This question was investigated in [47] using aluminum as an example. It turned out that quite early, at $T_e \approx 1$ eV, the rapid (quadratic) increase in frequency (14) is saturated. At temperatures above this one, the frequency (14) increases, but much more slowly.

A one-band metal was considered in [47]. Subsequently, complex cases with transition metals were analyzed in our works. In such metals the conduction band is formed from the *s*, *p*, and *d* bands.

The techniques of quantum-mechanical calculations using the density functional theory were mastered and the electronic spectra (the density of electronic states as a function of energy) of several metals were calculated (see the papers listed above). An approach called the two-parabola approximation was developed for *d* metals. In this approximation the calculated electronic spectrum is fitted by two parabolas. One parabola corresponds to the *s* or *sp* band of the electronic spectrum. The second parabola fits the *d* band [49, 103]. The two-parabola approach allowed the thermal conductivity κ and the electron–ion heat exchange coefficient α to be calculated in the tau approximation for a number of *d* metals [49, 103].

In an approximation simpler than (13) the thermal conductivity is written as

$$\kappa = \kappa_{rt}T_e/T_i, \qquad (15)$$

where κ_{rt} is the thermal conductivity at room temperature. Formula (15) is applicable in the case of ultrashort pulses at the two-temperature stage if the expansion of matter may be neglected. The meaning of Eq. (15) is simple. The numerator arises due to the increase in electron-gas heat capacity, while the denominator is related to the scattering by phonons. Above the Debye temperature the frequency ν_{ei} of this scattering is proportional to the lattice temperature:

$$\nu_{ei} \propto T_i. \qquad (16)$$

An obvious shortcoming of Eq. (15) compared to Eq. (13) is that the scattering by electrons is ignored. Accordingly, Eq. (15) is applicable in a limited range of temperatures, as a rule, below $T_e = (5–10)$ kK. Note an interesting fact. Although Eq. (13) takes into account the frequency ν_{ee}, the influence of this frequency on the conductivity κ begins where the approximation (14) ceases to be valid. However, here we would like to note another, more subtle fact.

The point is that Eq. (16) breaks down in the case of d metals with an incompletely filled d band. More specifically, it turns out that the coefficient of proportionality in Eq. (16) depends on the electron temperature T_e [102]. This dependence is very significant if the upper edge E_2 of the d band exceeds the Fermi energy only slightly: $E_2 - E_F \ll E_F$. In the segment from the Fermi energy to the edge E_2 the d states are empty at low temperatures T_e. For example, nickel, platinum, and palladium belong to metals with small E_2 [112]. The calculations in [102] show that the coefficient of proportionality in (16) decreases sharply at $T_e \le E_2$. The high values of this coefficient (at $T_e \ll E_2$) for metals with small E_2 are attributable to the high density of empty states near the Fermi level (Mott's effect [102]). At $T_e \sim E_2$ these states cease to be empty.

Unfortunately, the two-temperature thermal conductivity of each metal has to be calculated individually. Let us apply the technique described above to calculate the thermal conductivity of ruthenium—an important refractory metal that is applied, for example, in present-day photolithographic machines (see Section 3.7 about the ASML Company). The results of our calculations are shown in Figs. 3 and 4. The thermal conductivity κ is calculated in two steps. First, the thermal resistance caused by the scattering by the ion subsystem is found. Then, the electron–electron contribution to the resistance is determined. Next, the resistances are added, as for two series-connected conductors.

The total resistance asymptotically reaches the ion resistance at low temperatures T_e. Indeed, there are few excited electrons at such temperatures. Therefore, the electron–electron contribution to the resistance is negligible. In contrast, at high temperatures T_e the electron–electron scattering dominates.

3.5. On the Internal Heat Flow from Hot Electrons to the Ion Subsystem

The energy transfer from hot electrons to ions is proportional to the energy exchange coefficient α (5) between the electron and ion subsystems. Many papers are devoted to calculating the coefficient α. In our approach with the two-parabola approximation of the electronic spectrum the coefficient α is calculated separately for the s- and d-band electrons [49]. Thus, the total value of α is a sum of the partial contributions, $\alpha = \alpha_s + \alpha_d$.

Note also the important paper [113] (see Ch. 4 and Fig. 4 in it), where the coefficient α was calculated for a nonmetallic material, i.e., for a material with a gap in the electron energy spectrum (wide-bandgap LiF insulator). The dependence $\alpha(T_e)$ for an insulator differs qualitatively from the case of a metal. At low temperatures T_e there are few electrons in the conduction band and, therefore, the heat transfer power $\alpha(T_e - T_i)$ to the ion subsystem (per unit volume) is low.

3.6. Newton Rings

Above we have outlined the questions referring to the physics of two-temperature states. These include the system of two-temperature hydrodynamic equations (1)–(7), the two-temperature equations of thermodynamic state (Section 3.2), the two-temperature thermal conductivity (Section 3.4), and the energy exchange coefficient between the electron and ion subsystems in condensed matter (Section 3.5). The shortness of ultrashort laser action is responsible for the formation of two-temperature states. Since the propagation of heat through the near-surface layer of thickness d_T is supersonic (see Section 3.3), the acoustic motion of this layer lags behind the heating time. This lag has important hydrodynamic consequences.

It turns out that an ultrashort flash "instantly" (for sound) forms a heated layer, i.e., the mechanically passive material at rest with zero pressure is "instantly" converted into a material with a fairly high pressure. Of course, such a material on sound time scales $t_s = d_T/c_s$ begins to unload in two directions (momentum conservation law). The unloading toward the target generates a compression wave in the target, while the unloading toward the vacuum (or a different medium adjacent to the target with a low acoustic impedance) is a rarefaction wave. The formation of tensile stresses is associated with the rarefaction wave. The generation of discontinuity nuclei, i.e., voids in condensed matter (nucleation), begins at their sufficient (but not too large) amplitude exceeding the tensile strength of the material.

This generation ends with the detachment of a near-surface layer with a thickness of the order of d_T from the main body of the target. This phenomenon was developed in our department [1, 100, 114–118] and is now well known in the literature [81, 82, 119–122]. Calculations show that the ablation threshold (this is how the detachment of matter is called in laser applications) is higher than the melting threshold by a factor of 2–3. Therefore, the detachment occurs in a melt and is called cavitation. Indeed, at great excesses above the melting threshold (by several times) the crystal turns out to be strongly overheated in ion temperature. Under such conditions the melting proceeds rapidly, in atomic times. Then, there is an already formed near-surface liquid layer on the sound time scale.

Note the subtle dependence on super- and subthreshold. The surface tension and the balance between capillarity and melt recrystallization rate begin to play an important role. For example, this leads to the formation of a near-surface porous layer from nanocavities frozen into the solid matrix [123, 124].

The first clear (and unexpected) manifestation of the thermomechanical nature of laser ablation under ultrashort laser action was found in the remarkable 1998 paper [125] of D. von der Linde's group from Essen. The appearance of interference Newton rings, whose number on the illumination spot increased with time, was observed. In this connection, at the beginning it was suggested to attribute this phenomenon to the creation of some transient phase of matter whose optical characteristics differ greatly from the standard ones and, besides, change with time.

In our department we have managed to explain this phenomenon using the concepts of thermomechanical ablation, cavitation, and spallation [1, 100, 114–118]. This is how the concept of nanospallation appeared: light passes through the spallation plate twice; hence, its thickness is of the order of or smaller than the skin layer thickness of 10–20 nm for the optical frequency range. This picture of ablation then turned out to be unexpected for the physicists studying the laser–matter interaction. The point is that the views of evaporative ablation at moderate-intensity laser fluxes were familiar.

3.7. X-ray Sources

Many works have been carried out in our department on X-ray lasers [79, 113, 126–141]. They refer to the ablation by ultrashort pulses. A laser with a photon energy of 90 eV and a pulse duration of 7 ps was created at the Kansai Photon Science Institute. Our department performs joint studies of the applications of X-ray laser ablation with the strong laser group of this institute and in collaboration with the extreme-state matter diagnostics laboratory at the Joint Institute for High Temperatures of the Russian Academy of Sciences. The photon energy of 90 eV is close to the photon energy of 92 eV used in a "tin lamp". This is a light source for modern photolithography on nanometer scales; see ASML (https://www.asml.com/) for the TWINSCAN NXE:3400B machine operating at a wavelength of 13.5 nm already supplied to the customers. The fragmentation of a liquid tin droplet by a laser pulse in a tin lamp was investigated in [140, 141]. A droplet with a diameter of tens of microns falls from the doser and is broken into tiny fragments by a laser impact. The range of energies ~100 eV is attributed to the soft X-ray band or the extreme ultraviolet.

In addition, the work with the SACLA (Spring-8 Angstrom Compact Free Electron Laser) group of the RIKEN organization in Japan is carried out. The action of a sharply focused laser pulse with a toroidal intensity distribution over the spot (the vortex beam formed by a helical Fresnel-zone plate) on complex targets (laminates) has been investigated. The beam has record parameters: a spot diameters of ~1 μm, a pulse duration of 10 fs, and a hard X-ray photon energy of 7.71 keV [139].

3.8. Chaotic Surface Structuring

Chaotic micro-nanostructuring of a surface by ultrashort pulses has been detected experimentally [142–146]. This phenomenon was developed in many succeeding studies, because it has a huge spectrum of important applications. These include the specified variation of optical surface characteristics, the use of fabricated metasurfaces as highly sensitive sensors, the change in catalytic properties, wettability, and friction coefficient (tribology).

Micro- and nanostructures with spatial scales of 10–100 nm (less than the optical wavelength) amplify sharply the weak electromagnetic fields incident on the surface [91]. Amplification takes place in tiny local volumes at the sharp points of metallic structures (capillary nanodroplets crowning frozen jets) and in close gaps between neighboring surface convexities. The blackening of well-reflecting metals [142, 143] and the dramatic changes in permittivity (metasurfaces) are associated with this phenomenon. High-amplitude point electric fields enhance the Raman effect and photoluminescence [91]. The application of structured surfaces in highly sensitive sensors is based on this [91]. The sharp fractal increase in area and the nanorelief are responsible for the high catalytic activity and the variation of wettability (lotus leaf effect) and friction.

The works of our department were the first that explained the physical causes of the formation of micro-nanostructures [70, 77, 100, 104, 116, 123, 147–153]. We tied together the ultrashort pulse action, melting, thermomechanical nucleation, the foaming of a hot metal melt, foam expansion, the formation of foam in the form of a set of Voronoi cells (cells bounded by flat faces), the rupture of membranes together with the crystallization of membrane rupture remnants on the target surface. Under strong laser actions the foam has several clearly visible tiers. Initially, the first tier of bubbles and, subsequently, the second one are formed as the wave of tensile stresses propagates into the volume from the irradiated surface. The number of tiers increases with absorbed energy, but there are no more than two or three tiers.

Under strong laser actions the upper potions of the heated material (they were closer to the surface) expand in the form of a two-phase vapor–liquid mixture. The foam tiers expand with a velocity lower than the expansion velocity of the upper portions. They expand under the upper portions. At the initial stages the temperature of the material in the tiers is in the range between the melting and critical temperatures. It is this sequence of phenomena that ends with the crystallization of first-tier foam remnants and the formation of a surface micro-nanorelief.

We will add that to produce chaotic structures, it is necessary to achieve significant tensile stresses leading to cavitation. This requires that the laser pulse duration τ_L exceed the sound time scale $t_s = d_T/c_s$ not too much. The quantity t_s depends on the material. This time scale is especially large in the case of gold, t_s = 30–50 ps, because of the large heating depth, d_T = 100–150 nm, and the low speed of sound, $c_s \approx 3$ km s^{-1}. The heating depth in gold turns out to be large, because the two-temperature relaxation is slow, while the thermal conductivity is great.

In our calculations for gold in water [154], we compared ultrashort pulses with $\tau_L < 1$ ps, intermediate-duration pulses with $\tau_L = 50$ ps, and a long pulse with $\tau_L = 0.5$ ns; τ_L is the time it takes for the intensity to decrease by a factor of e: $I(t) = I_0\exp(-t^2/\tau_L^2)$. In the case of an intermediate duration, cavitation begins later than it does in the case of an ultrashort impact. The main thing is that there is no cavitation in the case of a long pulse. Accordingly, there is no foam, its breaking, and remnant freezing. Consequently, there will be no chaotic surface structures. Thus, the boundary that separates the fundamentally different solidified final surfaces runs between the intermediate and long pulse actions.

4. SHOCK WAVES

The research direction related to acoustic and shock waves is important. A huge amount of work on this direction has been done in our department. The subject is complex, has many branches, and is intertwined with dynamical phenomena. The dynamics is determined by both the generation and formation of shock waves (molten-zone passage, wave breaking) and the hydrodynamic consequences of their propagation (the compression and motion of a medium, phase transformations in materials under pressure).

The internal structure of shock waves in gases and condensed media (liquids and crystals) has been studied [115, 155–161]. The structure appears due to viscous and diffusion processes and due to relaxation of vibrational degrees of freedom [155, 157, 159]. In other cases, the front broadening is attributable to the excitation of molecules, ionization, and chemical reactions [155, 162]. There is a minimum scale in the condensed phase—the interatomic distance [115, 158–161]. The relaxation in crystals proceeds in a complicated way. In particular, a dependence on the crystal lattice orientation relative to the shock front appears [115].

A set of questions pertaining to radiative shocks have been analyzed. Here we say “radiative” not in the sense that part of the pressure behind the shock front is related to the radiation pressure. We talk about the structure of the ionization jumps maintained by the absorption of the laser radiation passing through a transparent gas and incident on an ionized layer [163–165]. The gas absorptivity changes due to ionization.

The propagation of shock waves in a plasma has been investigated. In a rarefied hot plasma the kinetic particle mean free path is great and “collisions” effectively appear due to the growth of plasma instabilities (the two-stream, Weibel ones). Therefore, the shock structure is associated not with the familiar real collisions of particles, but with the chaotic electric fields generated through plasma instabilities—collisionless shocks [166].

Much attention has been given to strong-explosion problems. Sedov’s exact solution is a classical one. However, it was obtained for an ideal gas with constant heat capacities. The question arises as to what a strong explosion or a short impact of Zeldovich and Weizsäcker will be in real media. This problematics has been studied in detail in various works of the department under the leadership of S.I. Anisimov [162, 165, 167–169] (a strong explosion and applications of the strong-explosion theory) and [170, 171] (a short impact—the influence of condensed-phase characteristics).

The questions about the influence of the equation of thermodynamic state on shock waves (for example, the hydroacoustic instabilities of shock waves) and about the determination of the equation of state using shock waves are very important. The papers [8, 9, 172] are devoted to using laser shocks to find the shock (Hugoniot) adiabat and the equations of state. The studies referred to the generation of powerful shock waves with amplitudes of a few or tens of megabars [9, 173].

The question about the gasdynamic instabilities of shock waves due to peculiarities of the equation of state and, accordingly, the Hugoniot adiabat has been studied in detail [174–180]. Unstable and neutrally stable regimes were found to exist. The corresponding regions of the phase diagrams for materials were determined. The emission of acoustic waves and entropy-vortex modes was described. These phenomena are similar to those that are observed under detonation. Similar acoustic processes also take place during the passage of a shock wave through the density jump at a contact of two gases (Richtmyer–Meshkov instability).

There are the interaction of a shock wave with the target rear boundary and accompanying spallation phenomena [173]. The spallation phenomena are intimately connected with “dusting” processes. This is how the Richtmyer–Meshkov instability played out at the interface between two media (a solid or liquid condensed medium and a vacuum) when the shock wave reaches the boundary is called.

The collision dynamics of two supersonic flows with the formation of two shock waves and a contact boundary has been investigated. The question abound the contact stability has been considered [181, 182].

In addition to a strong explosion and a short impact discussed above, many dynamical phenomena are associated with shock waves. The convergence of a shock wave to the center has been studied in various works of our department for cumulation and implosion problems and for the generation of thermonuclear neutrons [10, 183].

Another range of shock-wave phenomena is associated with the breaking of barriers and the formation of impact craters under a high-velocity impact of particles (see Section 2).

The range of moderate pressure amplitudes, a few—tens of GPa, is of great interest for present-day technological applications [60, 80, 184—195]. Many works on this extensive subject matter have been performed in our department. The formation of initially a compression wave and subsequently a shock wave on exposure to an ultrashort pulse has been studied. The plasticity threshold has been shown to be greatly shifted upward in the direction of increasing strength under ultrashort laser action [60, 185—188, 190, 194, 196—198]. Therefore, the shock waves remain elastic even under loads exceeding those at which the crystal transition to a plastic state occurs under impacts by more traditional means (plate throwing) by an order of magnitude.

Our studies have continued in collaboration with the Joint Institute for High Temperatures of the Russian Academy of Sciences for many years [60, 70, 74—78, 86, 104, 116, 123, 149—153, 184, 194, 196, 199—216]. In particular, delicate experiments with highly sensitive equipment have been carried out at this department using films of aluminum, iron, vanadium, tin, and other materials. The passage of laser shock waves through a film has been investigated for more than ten years [184, 185, 211, 217—219]. G.I. Kanel (Joint Institute for High Temperatures of the Russian Academy of Sciences) has made an important contribution to the work on shock waves on films. Kanel connected the data obtained under ultrashort loads with his measurements using VISAR on millimeter targets [211, 218—220]. As a result, the dependences were obtained in a very wide range of strain rates, from 10^5 to 10^9 s^{-1}. It was shown that at ultrahigh strain rates the strength of metals approaches its limiting values that are determined by the interatomic interaction [211, 218—220].

A new regime of existence of elastoplastic shock waves has been discovered [60, 187, 192, 193, 196, 197]. The regimes of shock propagation in solids are now classified as follows: (I) purely elastic waves; (II) elastoplastic shock waves in which the elastic wave velocity is greater than the plastic wave velocity; (III) elastoplastic shock waves that travel as a whole with a single propagation velocity [60, 187, 192, 193, 196, 197]; and (IV) purely plastic shock waves. Regime III was previously unknown.

4.1. The Single-Wave Elastoplastic Regime of Propagation

We will consider the question about the boundaries of existence of regime III. Figure 5 shows the “hydrostat” curve for the triaxial uniform hydrostatic compression of an elastoplastic body. The elastoplastic structure propagating with a single velocity is represented by the Rayleigh straight line. The corresponding straight line crosses initially the elastic Hugoniot adiabat (H_{elast}) and subsequently the plastic one (H_{plast}). The pressure on the piston that maintains the propagation of this stationary structure is equal to the pressure at the point of intersection of the Rayleigh straight line and the plastic shock adiabat.

Let d be the distance between the elastic and plastic jumps in regime III. Regime III passes into regime IV when the distance d is reduced to the lattice constant. In this case, the propagation speed is equal to $D_{\mathrm{elast}}|_{\max}$ (see Fig. 5). The corresponding pressure on the piston is 40—65 GPa in the case of aluminum [187].

Let us calculate the pressure on the piston at the boundary of regimes II and III. The plastic Hugoniot adiabat is

$$u_s = c_{\mathrm{plast}} + a_{\mathrm{plast}} u_p. \tag{17}$$

In Eq. (17) u_s is the speed of the single-wave structure and u_p is the speed of the piston maintaining the single-wave structure. For aluminum the plastic speed of sound is $c_{\mathrm{plast}} = 5.35$ km s^{-1} and the coefficient $\alpha_{\mathrm{plast}} = 1.37$ [185, 187, 211].

At the boundary of regimes II and III the speed u_s of the single- wave structure decreases to the elastic speed of sound c_{elast}. Substituting the elastic speed of sound for aluminum $c_{\mathrm{elast}} \approx 6.5$ km s^{-1} into (17), we determine the piston speed at the II/III boundary:

$$u_p|_{\min} = (c_{\mathrm{elast}} - c_{\mathrm{plast}})/a_{\mathrm{plast}} = 840\ \mathrm{m\ s^{-1}}. \tag{18}$$

The compression behind the plastic shock wave in the case of (18) is

$$\left(\frac{V}{V_0}\right)_{\mathrm{plast}|\min} = 1 - \frac{u_p|_{\min}}{c_{\mathrm{elast}} + a_{\mathrm{plast}} u_p|_{\min}} = 0.87, \tag{19}$$

where $u_p|_{\min}$ is given by relation (18).

The pressure on the piston at the II/III boundary is

$$p_{\mathrm{plast}}|_{\min} = \rho_0 c_{\mathrm{plast}}^2 \frac{1 - (V/V_0)_{\mathrm{plast}}|_{\min}}{[1 - a_{\mathrm{plast}}(1 - (V/V_0)_{\mathrm{plast}}|_{\min})]^2} = 14.9\ \mathrm{GPa}. \tag{20}$$

In Fig. 5 this is the pressure at the point of intersection of the plastic shock adiabat H_{plast} and the Rayleigh straight line referring to the elastic speed of sound c_{elast}. The value of (20) specifies the lower bound for the range of existence of the single-wave structure. The distance d separating the elastic and plastic jumps is great in the case of (20), larger than the interatomic distance by many orders of magnitude.

4.2. Residual Strains and Stresses after Ultrashort Laser Action

The problems pertaining to ultrashort laser pulses were discussed above, in Section 3. In Section 4 we consider shock waves. Let us present the results concerning the residual strains and stresses after the impact of an ultrashort laser pulse. As was said in Section 3.8, the formation of surface structures is associated with such laser actions. Nanoporous subsurface structures are formed under laser actions near the ablation threshold (slightly below the threshold) (see Section 3.8).

Here we present our new results that describe the state of a metal below the porous layer. We are interested in the residual strains and stresses that a strong shock wave leaves behind. The shock wave is formed in the high-pressure near-surface layer that emerges on time scales of the order of $t_s = d_T/c_s$ after ultrashort laser action. For aluminum this time scale is 20 ps.

The formation of a compression wave, its propagation into the volume of a semi-infinite target, and the compression wave breaking have been investigated adequately. The question arises as to what asymptotic state of a ductile metal is after the shock wave has gone to infinity. Under weak laser actions (well below the melting threshold) the metal returns to its initial state: first, the heated layer cools down and, second, the elastic compression wave leaves no residual strains. The laser actions with an amplitude near the ablation threshold cannot be deemed weak. A hot molted layer emerges under such laser action; the amplitude of the tensile stresses is sufficient to initiate cavitation.

Figure 6 shows the situation at the transonic (t = 51.2 ps ~ t_s) stage after laser action slightly below the ablation threshold for aluminum: below the ablation threshold there is no thermomechanical detachment of the material, although cavitation takes place if the nucleation threshold is exceeded. The absorbed energy is 70 mJ cm^{-2}. There is a sufficiently powerful shock wave behind which the formation of plastic deformations begins. Figure 6 and the succeeding figures present the results of large-scale molecular-dynamics simulations—the number of atoms is ~400 million. The flat-plate thickness is 500 nm. The system's sizes are 500 × 500 × 24 nm^3. The boundary condition that transmits the acoustic disturbances without their reflection acts at the right boundary of the layer. Thus, our statement is equivalent to the laser action on a semi-infinite target.

The development of residual strains and stresses is presented in Fig. 7. The shock wave has long left the layer under consideration through the right boundary $x = 500$ nm. The instant corresponding to Fig. 7 is $10t_s$. The ongoing processes include, first, the heat removal from the hot surface layer. At the boundary separating the liquid and solid phases there is a density jump (cf. mark *2* in Fig. 6). Second, the residual stresses evolve. Note the formation of a special thin solid layer near the solid–liquid interface itself. This special layer is marked by number *1* in Fig. 7.

The evolution of the stresses within the layer for $x < 500$ nm is traced in Figs. 8 and 9. We see how a sufficiently powerful shock wave traverses the layer under consideration and leaves it, going into the target. The rarefaction wave goes away from the layer under consideration behind the shock wave. The rarefaction wave is known to be formed due to the breakup of a high-pressure layer into two d'Alembert waves. One of the d'Alembert waves goes into the metal, while the other one is reflected from the free target boundary, changes its sign (from compression to extension), and propagates behind the compression wave.

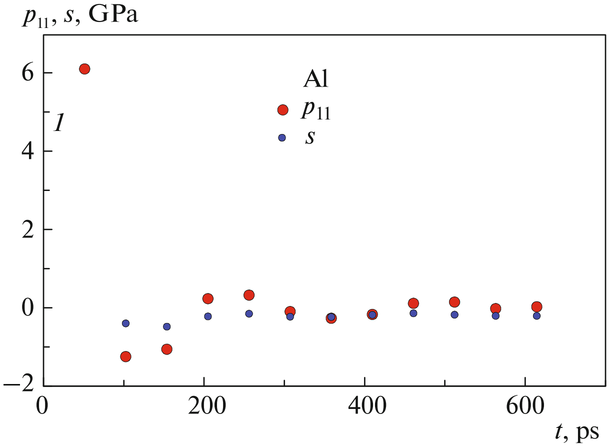

Fig. 8. (Color online) The maximum (in absolute value) longitudinal pressures p_{11} (taken with their signs) in aluminum are indicated by the big red circles. We see the shock passage over the layer $x < 500$ nm—the first red circle with a pressure of 6 GPa (cf. the profile in Fig. 6). The shock wave then goes into the target. The rarefaction wave travels over the layer. The second and third red circles correspond to the extensions. On long time scales the longitudinal pressure decreases to zero, because the layer under consideration borders the vacuum.

The evolution of the stresses continues after the escape of the combined acoustic (the amplitudes are small compared to the bulk modulus) disturbance from our layer (see Fig. 9). This combined disturbance consists of compression and rarefaction waves. The amplitude of acoustic disturbances is large enough to initiate the motion of dislocations. The quasi-asymptotic state of the layer is shown in Figs. 10 and 11.

The quasi-asymptotic state (see Figs. 10 and 11) is reached on long time scales after the escape of acoustic disturbances. The time shown in these two figures corresponds to 30 sound time scales t_s. There remain the frozen-in bubbles and the metal composed of tiny crystallites around bubbles. This layer is shown by the dark-green color in Fig. 11b due to the very small crystallite sizes (a few nanometers). The change of sign of the shear stress in Figs. 7 and 10 refers precisely to this special layer, but the strains (the thin green lines in Fig. 11) and stresses (see Fig. 10) also remain in the underlying layer.

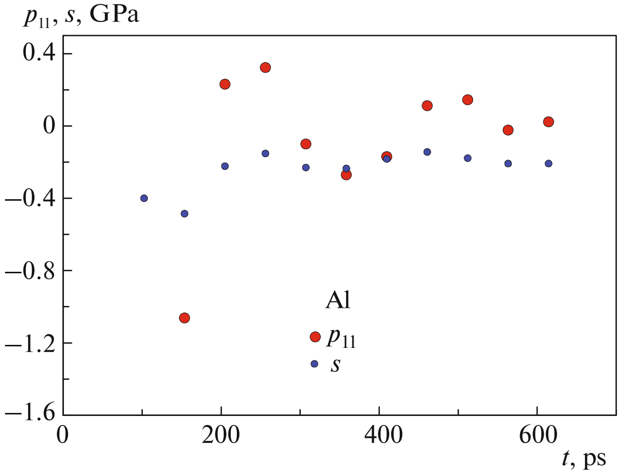

Fig. 9. (Color online) Reduction in the longitudinal pressure in aluminum with time to zero—this is the longitudinal loading process (see the caption to Fig. 8). The residual stresses in transverse directions inside the layer (outside the special layer *1* in Fig. 7) reach their quasi-stationary nonzero values. The formation of a residual strain field is associated with them.

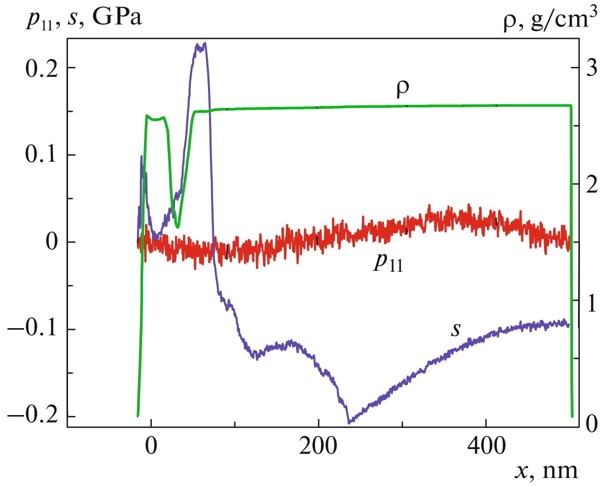

Fig. 10. (Color online) Complete aluminum solidification $t = 614$ ps. The longitudinal pressure decreases almost to zero, but the transverse stresses remain at a significant level of ~200 MPa. The special layer marked by number *1* in Fig. 7 also remains after the solidification of nanocavities inside the solid matrix.

5. THE PHYSICS OF A HYPERVELOCITY IMPACT AND A DUST-IMPACT MASS ANALYZER

Many physical problems are associated with the studies of Halley's Comet (see Section 2). In Section 2 we presented the results on dust protection and the Photon instrument (analysis of large cometary dust grains based on the masses and arrival times at Photon). These results were obtained owing to the collaboration of the research team under the leadership of V.E. Fortov and the physical hydrodynamics department of the Landau Institute for Theoretical Physics. Another very important aspect of the space mission referred to an analysis of the chemical and isotopic compositions of dust (in particular, in connection with the hypotheses about the origin of life on Earth). The PUMA (dust-impact mass analyzer) instruments were installed onboard the interplanetary Vega 1 and 2 spacecraft and Giotto [221–229].

There exist several ways of investigating the chemical composition. There are instruments with ionization by laser irradiation and a clarification of the composition by processing the optical spectra of a flash. There are magnetic mass analyzers. These two types of instruments are difficult to use onboard spacecraft due to the large mass of lasers or magnets and their technical complexity.

An exceptionally original concept was proposed. For which purpose do we need external ionization sources (lasers, electron beams, arcs) when a dust grain is ionized due to a hypervelocity impact (the impact velocity is 80 km s^{-1}, see Section 2)? This is the first simplification. The second one is related to abandoning the optical spectra and the separation based on the charge/mass ratio (z/m) in a magnetic field. Instead, the electrostatic field produced by a grounded grid in the gap between the target and the anode, on the one hand, and the grid, on the other hand, is simply applied. A constant positive voltage is maintained at the target [224].

Ions are pulled from the plasma cloud by the electric field of a capacitor; the grid and the anode act analogously to the capacitor plates. The higher the z/m ratio of an ion, the greater the velocity with which it escapes beyond the grid. The escaped ions are directed to the first time-of-flight tube of the mass reflectron. To increase the mass resolution of the instrument, PUMA was made in the form of a mass reflectron. The reflectron consists of the first tube, a reflector, and the second tube [222, 224, 227]. An ion collector recording the ion arrival time at the collector is installed at

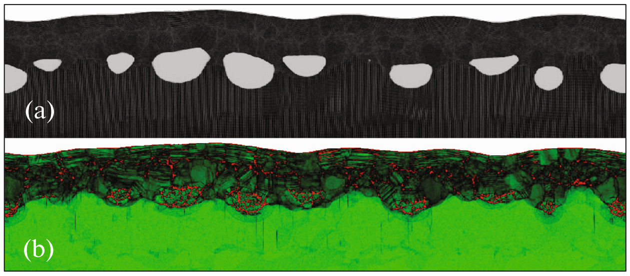

Fig. 11. (Color online) Maps of the density (a) and symmetry parameter (b) at 614 ps. The remnants of nanobubbles solidified in the solid matrix are seen. The symmetry parameter decreases at the dislocation boundaries (dark lines).

the end of the second tube. The time reading is launched by the optical flash from the arrived dust grain.

Faster ions from the group of ions with the same *z*/*m* ratio fly deeper into the reflectron with an electric field repelling a positive charge. Therefore, faster ions stay in the reflectron longer. This greatly narrows the line in the mass spectrum referring to a given *z*/*m* group.

In [221–229] the PUMA operation efficiency was analyzed and various ways of optimization were proposed, for example, the application of steps on a silver target plate. The problems of high-velocity impact physics and spectrum deciphering were solved. The line broadenings and spectrum distortions are related to the final ion escape distributions in angle and velocity and, most importantly, to the action of the space charge of the plasma cloud made of the grain and target materials. The electrostatics of the space charge screens significantly the external pulling capacitor field and has an effect on the time of ion charge pulling from the cloud [221–224, 226].

Results of the mission. The PUMA instruments onboard the Vega 1 and 2 and Giotto spacecraft allowed information on the physical and chemical characteristics of cometary dust to be obtained for the first time directly (until this time there were only data from astronomical observations). It emerged that the concentration of dust grains with masses less than 10^{-14} g and sizes less than 100 nm (nanodust) is much greater than was predicted by the cometary coma models. Another very important observation, in addition to the abundance of nanodust, was the detection of organics. It turned out that most of the dust grains are highly enriched by light elements, such as hydrogen, carbon, nitrogen, and oxygen. The observational data provide evidence for the models that describe the cometary materials as ices that passed serious radiation treatment.

The formation of an electron jet was detected [223]. Such a jet is formed in the case of a plasma cloud in an external electric field of opposite polarity, when the external field pulls electrons from the cloud (the cloud on the cathode). The electrostatic potential relief was shown [223] to have a saddle point due to the combined field (the external one plus the space charge).

This point is analogous to the saddle points in the combined field of the gravitational and centrifugal potentials of two masses rotating around a common center of mass. The outflow of electrons from the cloud occurs through the saddle point and, therefore, has the pattern of a collimated jet. Note that a rotating system of two gravitating points has five saddle points called the Lagrange or libration points. The matter in a binary system with a filled Roche lobe is known to be transferred in the form of a jet through the inner Lagrange point. For example, the accretion in low-mass binary systems proceeds in this way.

6. ASTROPHYSICS

The plasma and lasers department of the Landau Institute for Theoretical Physics of the Russian Academy of Sciences has carried out a number of works on astrophysics. The studies were performed in collaboration with R.A. Sunyaev at the Space Research Institute of the Russian Academy of Sciences and the Max Planck Institute (MPI) for Astrophysics [230–234]. The contact attachment of an accretion disk to a neutron star with a weak magnetic field, which is unable to move the disk away from the stellar surface and to create a magnetosphere in the gap between the disk and the surface, was described. It turned out that a swirling flow moves over the surface due to the accretion of disk angular momentum onto the surface [230, 233]. This flow gradually transfers its angular momentum to the star, with appreciable differential rotation propagating to rather significant depths.

The flow width in polar angle, which is measured from the equatorial plane, is proportional to the accretion rate. The higher this rate, the higher the latitudes to which the flow rises. This is because of the local constraint on the Eddington radiative cooling power.

Previously, the statement with the contact of a rapidly rotating (a significant fraction of the Keplerian velocity on the stellar surface) flow along a belt of finite width in polar angle was not considered. Instead, a disk in the spirit of the Shakura–Sunyaev solution [235] was considered, while the mechanical interaction with the star was introduced into this solution using the boundary condition on the disk that was set on the stellar surface [236]. The rotating flow moves above the stellar surface with a supersonic speed [230, 233, 237]. The interaction with the star occurs through turbulent friction [230].

Determining the velocities of the plasma filling the intergalactic spaces in clusters of galaxies is of great importance. These velocities are related to the large-scale motions and turbulence [131]. As a result, a significant hydrodynamic broadening of X-ray emission lines occurs. It is quite possible to measure line widths of a few electronvolts from a practical point of view for present-day X-ray space observatories with cryogenic detectors. Measuring the line shape and width gives valuable information about the intergalactic velocity field and, consequently, the global distribution of masses and dark matter, the cooling flows, and the shock waves generated by relativistic jets from the central object.

In our paper [231] we used the spectral representation of the inertial range of a Kolmogorov cascade transferring the kinetic energy from large to small scales to calculate the radiation line shape. Observations and measurements of the kinematic Sunyaev–Zeldovich effect and the X-ray line profiles provide complementary information about the velocity field.

The accretion onto an M87-scale supermassive black hole was considered in [233]. The case where the accreting matter slowly (compared to the local speed of sound) rotates at the Bondi radius R_{B} is typical. Subsonic turbulence in the gas at distances that are great compared to the Bondi radius is responsible for the rotation. The angular momentum l of the accreting matter at the Bondi radius is small. Nevertheless, the rotation velocity of the matter increases as it settles (subsonic accretion) due to the conservation of specific angular momentum under accretion (i.e., as the matter settles from the Bondi radius to the center).

At the radius $r_c = l^2/Gm_{\mathrm{bh}} = M_{\mathrm{B}}^2 R_{\mathrm{B}}$ the gas rotation velocity is equal to the local centrifugal velocity (G is the gravitational constant, m_{bh} is the mass of the supermassive black hole, and M_{B} is the Mach number in rotation velocity at the Bondi radius). A centrifugal barrier is formed here, which reduces sharply the accretion rate compared to the maximum possible one [233]. The barrier is in the shape of a toroidal clump.

Turbulent friction begins to have an effect at the radius r_c; above this radius the gas settled with the conservation of specific angular momentum. As a result, inner and outer disks are formed. The matter sinks to the black hole over the inner disk, while the outer disk removes the angular momentum of the inner disk outward beyond the Bondi radius [233]. Part of the matter is ejected outward over the outer disk. This matter apparently forms vast dust clouds around M87 and quasars.

The times in which the angular rotation vector at the Bondi radius and, accordingly, the direction of the relativistic jets ejected from the central black hole zone changes (due to the variability of external turbulence) were estimated in [233].

In [234] we derived a relativistic formula for the energy of standing sound waves in a photon–baryon–electron plasma. The formula was obtained from simple hydrodynamic and thermodynamic relations. It is applicable for an arbitrary relation between the energy density of photons, the rest energy density of baryons, and the thermal energy density of baryons. The formula describes the transition between the extreme cases in a continuous way. The results of [234] are important for the description of sound waves in a photon gas in the early Universe.

7. LASER TECHNOLOGIES

Lasers are applied in many modern technologies. Here we will dwell on recent works of the plasma and lasers department in two directions. First, we will tell about the production of metasurfaces using point laser actions. Sharply focused laser actions, whereby the illuminated spot has sizes of the order of the optical radiation wavelength—illumination at the diffraction limit, are called the point ones here. Second, we will talk about the ablation into a liquid. This is a promising direction that allows nanoparticles with valuable properties for practical applications to be produced in an ecologically clean way.

7.1. Numerical Simulations of the Formation of Cupolas on Thin Films

The surface structuring, the creation of metasurfaces with artificial properties, has already been mentioned above (see Section 3.8). However, we considered the chaotic surfaces emerging under a sufficiently short (in time) and sufficiently intense laser action on bulk targets. Furthermore, it is important to emphasize that for a chaotic surface to be formed, the irradiation spot must be sufficiently large in sizes—at least tens of microns. No random structures are formed in small spots at the diffraction limit of laser radiation, because a significant excess of the spot diameter above the capillary scale is required; the sizes of chaotic structures are controlled by surface tension [70, 77, 104, 116, 123, 147, 150–153].

A series of point laser actions is used to create "cupola" arrays [91, 95] on thin films deposited on substrates. This is how a metasurface emerges [91, 95]. Here we talk about "cupolas" in inverted commas, because here we have in mind the figure created by a point laser action. This can be a really small rise of the film surface in the form of a roughly parabolic cupola, or this is a cupola with a frozen jet at the top, or the jet is sharp, then short, then a hole appears at the top of the cupola instead of the jet, next the hole expands in size plus a crown of frozen jets (nancrown) is formed around it, and, finally, a hole in the film becomes the figure created by the laser action. We passed through the sequence of solitary structures in the direction of increasing laser pulse energy [84, 88–96, 99, 238–243] by assuming the beam size on the target and other parameters (for example, the pulse duration) to be fixed.

Obviously, the degree of film modification in the irradiation spot increases from a slight swelling to a hole in the film increases with pulse energy. At even greater energies E the hole diameter $d(E)$ increases. However, as shown in [242], this is not accounted for by the laser beam wings (i.e., according Liu's formula [244]). An interesting idea was proposed in [242]. The shock wave that is generated in a substrate and propagates away from the irradiation spot, raising the film from below, i.e., from the substrate, provides an increase in the function $d(E)$. This shock action in the substrate is attributable to the lateral expansion of the substrate material at its boundary with the film.

A good approximation of the spatial profile of the laser beam in a direction transverse to its axis is the approximation by a Gaussian:

$$I(r) = I_0 \exp(-r^2/R_L^2), \tag{21}$$

where r is the cylinder radius measured from the beam axis; we assume that the beam is directed perpendicularly to the target surface. If the thermal or mechanical connection between the neighboring radii r and r' is neglected, then the variation of the local thermohydrodynamic situation in r is determined only by the change of the beam intensity (21) in r. If, in addition to what has been said, we assume that there is an ablation threshold $I_{\rm thr}$, then we arrive at Liu's formula [244] for the increase in ablation radius $r_{\rm thr}$ as the pulse energetics is enhanced (E and I_0 are proportional to each other).

Liu's formula is simple. Let us write $I(r_{\rm thr}) = I_{\rm thr}$ in (21). Taking the logarithm of the exponential (potentiation), we obtain

$$r_{\rm thr} = R_L\sqrt{\ln(I_0/I_{\rm thr})}. \tag{22}$$

In experiments I_0 is varied and $r_{\rm thr}$ is plotted against the logarithm [95]. The ablation threshold $I_{\rm thr}$ ($E_{\rm thr} \propto I_{\rm thr}$) and the beam radius R_L are determined in this way.

Relation (22) is applicable when the spot diameter $2R_L$ is much larger than the heating depth d_T (in the case of a bulk target) or the film thickness d_f. This is the case under an important condition: the ablation process ends at depths of the order of d_T or d_f. In the case considered in [242], this is not true. The shock wave goes to depths of the order of R_L and further. In the segment of depths up to R_L the shock amplitude decreases only slightly. Then, the shape of the shock wave and the flow behind the shock begin to be spherized at depths of the order of R_L, i.e., the shock goes into the volume and propagates sideways under the film along the film–substrate boundary.

In this case, on long time scales $t_{s2} = R_L/c_s$ the shock amplitude decreases, but as a power law, whereas, according to Eqs. (21) and (22), the Gaussian wings decay exponentially. Therefore, under strong laser actions (the energy E is great) the hole expansion in the film begins to be controlled on completely different time scales, not $t_s = d_T/c_s$ and $t_s = d_f/c_s$, but t_{s2}, and on different spatial scales, not d_T and d_f, but R_L. In this case, the hole expansion law changes fundamentally with increasing energy—the expansion is a power-law one [242] rather than logarithmic (22).

Above, we dwelt on the change in the degree of damage modification on a thin film with increasing absorbed energy; a thin film is the one whose thickness d_f is smaller than the heating depth d_T. We discussed the paper [242] describing the strongest damages. We talked about a solitary damage. It was noted that a metasurface is created from an array of such repeated damages ("cupolas"). The mutual influence of neighboring cupolas begins only when the spatial array step is reduced to a size of the order of R_L.

Let us briefly touch on the technique that allowed us to simulate the cupola creation process in [84, 88–96, 99, 238–243]. This is not a simple process. It includes several independent physical stages.

(1) The absorption of ultrashort pulse energy in a spot of radius R_L.

(2) The supersonic propagation (see Section 3.3) of the absorbed energy through the electron subsystem from the skin layer $\delta_{\rm skin}$ into the film, $d_f > \delta_{\rm skin}$ [97].

(3) The film is thin, $d_f < d_T$. In [97] we considered the turning of the heat flow from its propagation across the film (i.e., normal to the film plane) to lateral propagation, along the film (i.e., in tangential directions to the film surface). This turning occurs even at the two-temperature stage. This is important, because at this stage heat is transferred through the electron subsystem with a supersonic speed. Meanwhile, the succeeding film detachment from the substrate is mechanical in nature and occurs on sound time scales $t_s = d_T/c_s$; consequently, it lags behind the supersonic spatial redistribution of the heat initially stored in the skin layer. The amount of thermal energy brought to a given local place at the supersonic stage, i.e., as long as the film was almost stationary, determines whether the film will be detached or not in this place (see also the discussion at the end of Section 3.3 regarding the comparison of our theory for the turning of a supersonic heat flow with experiments [98]).

(4) Thus, the distribution of internal energy over the film space has been created (two-temperature heat conduction, Section 3.4, and electron–ion heat exchange, Section 3.5). Next the sonic stage of mechanical phenomena begins; $t_s = d_f/c_s \approx 17$ ps for a 50-nm-thick gold film, the two-temperature relaxation duration $t_{\rm eq}$ is of the order of a few picoseconds. A variation of the pulse duration τ_L from low values to 8 ps does not affect the formation of a cupola at R_L of the order of a few microns [245]. At such large R_L the expansion of the heating spot due to the heat flow turning is negligible.

The film is detached from the substrate when a gap Δ of several interatomic distances appears between the film and substrate boundaries. We have $\Delta \ll d_f \ll R_L$. Therefore, the detachment problem may be considered in the one-dimensional hydrodynamic approximation. After the film detachment the velocity of its local (over the film surface) center of mass does not change any more. We used our 1D–2T code to calculate the center-of-mass velocity $v_{cm}(r) = v_{cm}(F_{\rm abs}(r))$ [95] as a function of the local absorbed energy (the 1D–2T code is a one-dimensional, two-temperature hydrodynamic code [90, 239]). We also calculated the ion temperature distribution $T_i(r)$ at the film detachment stage.

(5) The mentioned distributions $v_{cm}(r)$ and $T_i(r)$ were used as input data for the molecular-dynamics (MD) MD–MC code (MK is the description of the thermal conductivity of a metal using a Monte Carlo unit) [84, 88–92, 95, 99, 238, 240, 241, 243]. The MD–MC code described only the motion of the film—therein lies the simplification of MD simula-

tions, because the substrate atoms need not be taken into account after the film detachment from the substrate. The mechanical action of the substrate outside the detachment spot was simulated using a thermostat that kept the film from moving outside the detachment spot.

(6) Colossal progress in understanding nonequilibrium and equilibrium processes is connected with MD. It turned out that “simple” hydrodynamic flows are described by MD beginning from several tens of interatomic distances (by “simple” we mean situations without slow relaxation). The most important limitation of the MD approaches is that the computational resources are limited—it is difficult to simulate condensed systems with a volume greater than a cubic micron (this is about a hundred billion atoms). Therefore, modern science follows the path of constructing multiscale models, where the bottom tier is MD, while the top tiers are constructed phenomenologically, through the dislocation and plasticity theories. However, only the necessary coefficients for the description of relaxation phenomena in terms of the traditional views of an elastically or plastically deformed solid body are extracted from MD on this path, i.e., we have to forget about the efficiency of applying MD to uncover the dynamics of events.

In [84, 88–92, 95, 99, 238, 240, 241, 243] we followed a different path. Direct MD simulations of the experiment [245] are difficult to perform; a film with sizes of 3×3 μm^2 and a thickness of 50 nm has a rather large (for MD) volume of about 0.5 μm^3.

Therefore, we used scaling and the similarity theory. This allowed the phenomena of cupola formation to be described on spatiotemporal scales smaller by a factor of 5–10. The similarity theory states: the flows are identical if the characteristic dimensionless parameters describing the problem statement are identical.

(7) The details of the scaling theory are presented in [84, 88, 89, 95, 240], where the problem was shown to be described with two dimensionless parameters: the capillary number $N_{\rm cap}$ and the thermal number N_T. We then took the real problem (e.g., [245]) and calculated the numbers $N_{\rm cap}$ and N_T. Next, the parameters of the MD–MC code were changed in such a way that these numbers were the same in the statement with numerical simulations.

This can be done. In the MC unit we reduced the thermal conductivity so as to fit the number N_T in our numerical experiment to the real one. The capillary numbers $N_{\rm cap}$ were reconciled using the parameter a. We increased the velocity by the same factor, $v_{cm}(r) \rightarrow av_{cm}(r)$. Here, the first velocity is the velocity from the 1D–2T-gd code, while the second one is the velocity put into the MD statement.

(8) The MD–MC code remarkably describes the entire sequence of events. This is the initial stage of motion with specified distributions of velocities $av_{cm}(r)$ and temperatures $T_i(r)$. This stage ends when the film traverses a distance comparable to the radius R_L along the normal. Next an interesting thing begins.

The capillary forces become important—indeed, a curvature of the detached part of the film appears (a cupola is formed). First, the film deceleration by surface tension and, second, the transfer of the film material over the film toward the cupola axis become significant together with the curvature. The transfer occurs, because there is a tangential component of the capillary force and it is directed toward the axis. The transfer causes the one-sided (upward from the cupola) or two-sided (upward and downward from the top of the cupola) jet at the top of the cupola to grow (see [84, 88]).

Let us compare the time of the detachment stage $t_s = d_T/c_s$ = 10–30 ps and the cupola formation time $t_{3D} = R_L/v_{cm}$. In our experimental situation we have $t_{3D} \sim$ 100 ns [246]. In our calculation $t_{3D} \sim$ 3 ns. We want to draw attention to the enormous difference in the time scales of the initial (t_s) and subsequent (t_{3D}) stages.

We emphasize that on time scales $t > t_{\rm eq}$ the two-temperature effects may be neglected; $t_{\rm eq} < t_s$. Accordingly, in our MD–MC computations we proceed from the reference values of the ordinary (i.e., one-temperature) thermal conductivity.

In the real problem the parameter $N_{\rm cap}$ and N_T are such that the cooling of the liquid phase constituting the film becomes significant approximately simultaneously with the action of capillarity on time scales of the order of t_{3D}. The cooling is attributable to the outflow of heat over the metal film from the heating spot to the cold periphery; the radiative losses and heat removal into the dielectric substrate are small.

In our numerical statement (because the pair of parameters, $N_{\rm cap}$ and N_T, is the same in both calculation and experiment) the mutual influence of the dynamics (capillarity) and cooling also takes place on time scales of the order of t_{3D}. Consequently, the cooling and freezing of the melt, on the one hand, and the capillary deceleration and jet formation at the top, on the other hand, compete at the stage t_{3D}.

This competition creates a fairly rich picture of the above-listed surface modifications (cupolas, nanocrowns), depending on the absorbed energy and the “play” of $N_{\rm cap}$ and N_T [93, 95]. The processes at work are described in detail in [84, 88–96, 99, 238–243]. Although the experiments with cupolas have been carried out since 2003–2004 [247], a quantitative picture with the motion of a liquid film stopped by crystallization did not exist previously.

Note that a radial corrugation of frozen cupolas is seen in the experiments [245]. The corrugation points to an interesting phenomenon. The motion of the cupola is not stopped instantly after solidification. The cupola continues to move by inertia toward the substrate. At the same time, the cupola is thin, because part of its mass was transferred to the jet. There is a plastic deformation of the thin cupola shell.

The area of the cupola should decrease as it moves toward the substrate; this happens if the film is liquid. However, we are dealing with a solid body in the form of a thin shell. No reduction of the area is possible. As a result, the area excess folds into corrugations.

The corrugations are unable to straighten out back. Plastic deformation absorbs the kinetic energy of the shell motion toward the substrate. The motion of the cupola in the corrugated state is stopped.

7.2. Plasmonics, Thermal Physics, and Hydrodynamics

Another direction of the works of our department is related to the solution of combined problems. The interference of a surface plasmon polariton with an incident laser electromagnetic wave gives rise to a nontrivial heating spot [3, 248, 249]. Hot and cold stripes alternate in this spot. The step between stripes is determined by the plasmon polariton wavelength, λ_{pp}. The heating is accomplished by an ultrashort pulse. A thin film $d_f < d_T$ is heated, with $\lambda_{pp} \times d_f$. The strategy worked out above is applicable under these conditions.

First the field distributions and the dependence of the energy dissipation power in the film skin layer are found using an electrodynamic code (first step). Then, the 1D–2T-gd code is switched on and the distribution of energy dissipation over the film surface $F_{\text{abs}}(y)$ is reprocessed into the distributions of the mechanical recoil velocity $v_{cm}(y)$ [238] and temperature $T(y)$; the coordinate y is directed along the film across the corrugation stripes (second step). In the third step, we find the final frozen corrugation shapes using the MD–MC code.

Note that such a corrugation is used to produce holograms [2, 248, 249].

7.3. Ablation into a Liquid

The processes during ablation into a liquid have been poorly studied from theoretical and computational standpoints. Therefore, the corresponding studies have been carried out in our department since 2016. The applied aspect of this problem can be studied from the first references in [59, 154, 250–254].

The works carried out in [59, 154, 250–254] allowed a number of previously unclear questions to be elucidated. Laser actions of various durations on a gold target immersed in water were considered. A variation of the durations τ_L from ultrashort (~1 ps) to intermediate (50 ps) and long (500 ps) ones affects significantly the pulse-induced situation [154]. In particular, the residual relief on the surface in the irradiation spot changes qualitatively. This fact was discussed above, see the end of Section 3.8.

The calculations of ablation into a liquid listed above were carried out using the two-temperature hydrodynamic and MD–MC codes. Note the paper [255], where a high-performance multiprocessor version of the SPH code (SPH stands for smoothed particles hydrodynamics) [256] was used for the problem simulations.

The duration of the acceleration stage of the metal–liquid contact boundary is of the order of the laser pulse duration. The end of the acceleration stage is followed by a prolonged deceleration of the contact boundary. The emergence of conditions under which the development of Rayleigh–Taylor hydrodynamic instability begins is associated with the deceleration. The pulse lengthening in time reduces the importance of instability development.

In the case of a laser action with enhanced energetics, the diffusion is more intense. In this case, the diffusion processes act toward the suppression of the Rayleigh–Taylor instability. In our works we studied the gold vapor condensation processes in a liquid in a layer of diffusive mixing. Condensation begins not simultaneously and not uniformly over the diffusion layer. As a result of condensation, gold clusters and then nanoparticles are formed.

The evolution of a flow up until the formation of a bubble in a liquid has been traced for the first time [154].

8. CONCLUSIONS

Above we described the present-day activity of the plasma and lasers department at the Landau Institute for Theoretical Physics organized long ago by the academician I.M. Khalatnikov. The researchers of this department are deeply grateful to Khalatnikov for the creation of the institute and its long-term efficient management. The department passed a glorious path marked by significant fundamental and applied achievements.

By no means all achievements found their reflection in the above list, for example, the works on the "maturation" of a thermal explosion or on the biophysical subject matter, the productivity of Biosystems, were covered insufficiently. We did not touch the works on studying a metal in a two-temperature state. The studies devoted to the nonlinear photoelectric effect, i.e., the emission of electrons under surface illumination, remained outside the narration.

REFERENCES

1. S. I. Anisimov, V. V. Zhakhovskii, N. A. Inogamov, K. Nishihara, A. M. Oparin, and Yu. V. Petrov, JETP Lett. **77**, 606 (2003).

2. B. J. Demaske, V. V. Zhakhovsky, N. A. Inogamov, and I. I. Oleynik, Phys. Rev. B **82**, 064113 (2010).
3. A. I. Ignatov, V. V. Zhakhovsky, A. M. Merzlikin, and N. A. Inogamov, J. Phys.: Conf. Ser. **1147**, 012068 (2019).
4. A. V. Bushman and V. E. Fortov, Sov. Phys. Usp. **26**, 465 (1983).
5. K. V. Khishchenko, S. I. Tkachenko, P. R. Levashov, et al., Int. J. Thermophys. **23**, 1359 (2002).
6. I. V. Lomonosov, Laser Part. Beams **25**, 567 (2007).
7. http://teos.ficp.ac.ru/rusbank/; http://www.ihed.ras.ru/rusbank/.
8. A. M. Prokhorov, S. I. Anisimov, and P. P. Pashinin, Sov. Phys. Usp. **19**, 547 (1976).
9. S. I. Anisimov, A. M. Prokhorov, and V. E. Fortov, Sov. Phys. Usp. **27**, 181 (1984).
10. S. I. Anisimov, V. E. Bespalov, V. I. Vovchenko, et al., JETP Lett. **31**, 61 (1980).
11. S. I. Anisimov, M. A. Berezovskii, M. F. Ivanov, et al., Phys. Lett. A **92**, 32 (1982).
12. S. I. Anisimov, M. A. Berezovskii, V. E. Zakharov, et al., Sov. Phys. JETP **57**, 1192 (1983).
13. S. I. Anisimov, M. A. Berezovskii, M. F. Ivanov, et al., Sov. Phys. Dokl. **26**, 510 (1981).
14. S. I. Anisimov, A. M. Bonch-Bruevich, M. A. El'yashevich, et al., Sov. Tech. Phys. **11**, 945 (1966).
15. S. I. Anisimov, Sov. Phys. JETP **27**, 182 (1968).
16. S. I. Anisimov, Ya. A. Imas, G. S. Romanov, and Yu. V. Khodyko, *The Effect of High Power Radiation on Metals* (Nauka, Moscow, 1970) [in Russian].
17. S. I. Anisimov and V. A. Khokhlov, *Instabilities in Laser-Matter Interaction* (CRC, Boca Raton, FL, 1995).
18. S. I. Anisimov, M. I. Tribel'skii, and Ya. G. Epel'baum, Sov. Phys. JETP **51**, 802 (1980).
19. S. I. Anisimov, S. M. Gol'berg, E. N. Sobol', and M. I. Tribel'skii, Sov. Tech. Phys. Lett. **7**, 379 (1981).
20. S. I. Anisimov, S. M. Gol'berg, O. L. Kulikov, et al., Sov. Tech. Phys. Lett. **9**, 99 (1983).
21. S. I. Anisimov, S. M. Gol'berg, B. A. Malomed, and M. I. Tribel'skii, Sov. Phys. Dokl. **27**, 130 (1982).
22. S. I. Anisimov, S. M. Gol'berg, and M. I. Tribel'skii, Sov. Phys. JETP **55**, 929 (1982).
23. S. I. Anisimov and M. I. Tribel'skii, Sov. Tech. Phys. Lett. **6**, 13 (1980).
24. S. I. Anisimov and A. Kh. Rakhmatulina, Sov. Phys. JETP **37**, 441 (1973).
25. S. I. Anisimov and V. V. Zhakhovskii, JETP Lett. **57**, 99 (1993).
26. V. V. Zhakhovskii and S. I. Anisimov, J. Exp. Theor. Phys. **84**, 734 (1997).
27. S. I. Anisimov, D. O. Dunikov, V. V. Zhakhovskii, and S. P. Malyshenko, J. Chem. Phys. **110**, 8722 (1999).
28. V. V. Zhakhovsky, A. P. Kryukov, V. Yu. Levashov, et al., Proc. Natl. Acad. Sci. U. S. A. (2018, in press). https://doi.org/10.1073/pnas.1714503115
29. S. I. Anisimov and Yu. I. Lysikov, Prikl. Mat. Mekh. **34**, 926 (1970).
30. S. I. Anisimov and B. S. Luk'yanchuk, Phys. Usp. **45**, 293 (2002).
31. S. I. Anisimov and N. A. Inogamov, JETP Lett. **20**, 74 (1974).
32. A. V. Turlapov, E. A. Kuznetsov, and M. Yu. Kagan, arXiv:1903.04245 [cond-mat.quant-gas] (2019).
33. S. I. Anisimov and B. I. Makshantsev, Sov. Phys. Solid State **15**, 743 (1973).
34. S. I. Anisimov and V. L. Komolov, Sov. Phys. Solid State **16**, 371 (1974).
35. I. V. Aleshin, S. I. Anisimov, A. M. Bonch-Bruevich, et al., Sov. Phys. JETP **43**, 631 (1976).
36. S. I. Anisimov, V. A. Gal'burt, and M. I. Tribel'skii, Sov. J. Quantum Electron. **11**, 1010 (1981).
37. S. I. Anisimov, B. I. Makshantsev, and A. V. Barsukov, Opt. Acoust. Rev. **1**, 251 (1991).
38. R. Z. Sagdeev, S. I. Anisimov, A. A. Galeev, et al., Adv. Space Res. **2**, 133 (1982).
39. S. I. Anisimov, A. V. Bushman, G. I. Kanel', et al., JETP Lett. **39**, 8 (1984).
40. V. A. Agureikin, S. I. Anisimov, A. V. Bushman, et al., Teplofiz. Vys. Temp. **22**, 964 (1984).
41. S. I. Anisimov, B. A. Demidov, L. I. Rudakov, et al., JETP Lett. **41**, 554 (1985).
42. S. I. Anisimov, V. P. Karyagin, V. A. Kudryashov, et al., JETP Lett. **44**, 615 (1986).
43. S. I. Anisimov, B. L. Kapeliovich, and T. L. Perel'man, Sov. Phys. JETP **39**, 375 (1974).
44. M. I. Kaganov, I. M. Lifshits, and L. V. Tanatarov, Sov. Phys. JETP **4**, 113 (1957).
45. B. Rethfeld, D. S. Ivanov, M. E. Garcia, and S. I. Anisimov, J. Phys. D **50**, 193001 (2017).
46. Yu. V. Petrov, K. P. Migdal, N. A. Inogamov, and S. I. Anisimov, JETP Lett. **104**, 431 (2016).
47. N. A. Inogamov and Yu. V. Petrov, J. Exp. Theor. Phys. **110**, 446 (2010).
48. B. Y. Mueller, I. Klett, and B. Rethfeld, AIP Conf. Proc. **1464**, 609 (2012).
49. Yu. V. Petrov, N. A. Inogamov, and K. P. Migdal, JETP Lett. **97**, 20 (2013).
50. L. D. Landau, *Collection of Scientific Works* (Nauka, Moscow, 1969) [in Russian].
51. A. I. Akhiezer, Zh. Eksp. Teor. Fiz. **8**, 1318 (1938).
52. V. A. Krasil'nikov and V. V. Krylov, Introduction to Physical Acoustics (Nauka, Moscow, 1984) [in Russian].
53. L. Waldecker, R. Bertoni, R. Ernstorfer, and J. Vorberger, Phys. Rev. X **6**, 021003 (2016).
54. A. M. Brown, R. Sundararaman, P. Narang, et al., Phys. Rev. B **94**, 075120 (2016).
55. P. Maldonado, K. Carva, M. Flammer, and P. M. Oppeneer, Phys. Rev. B **96**, 174439 (2017).
56. I. Klett and B. Rethfeld, Phys. Rev. B **98**, 144306 (2018).
57. S. Ono, Phys. Rev. B **97**, 054310 (2018).
58. S. Ono, arXiv:1901.04652v1 [cond-mat.mtrl-sci] (2019).
59. N. A. Inogamov, V. V. Zhakhovskii, and V. A. Khokhlov, J. Exp. Theor. Phys. **127**, 79 (2018).
60. N. A. Inogamov, V. A. Khokhlov, Yu. V. Petrov, et al., AIP Conf. Proc. **1426**, 909 (2012).

61. Yu. V. Petrov, K. P. Migdal, N. A. Inogamov, and V. V. Zhakhovsky, Appl. Phys. B **119**, 401 (2015).
62. K. P. Migdal, D. K. Il'nitsky, Yu. V. Petrov, and N. A. Inogamov, J. Phys.: Conf. Ser. **653**, 012086 (2015).
63. N. A. Inogamov, V. V. Zhakhovsky, V. A. Khokhlov, et al., J. Phys.: Conf. Ser. **500**, 192023 (2014).
64. Ya. B. Zeldovich and Yu. P. Raizer, *Physics of Shock Waves and High-Temperature Hydrodynamic Phenomena* (Fizmatgiz, Moscow, 1963; Academic, New York, 1966, 1967).
65. V. N. Zharkov and V. A. Kalinin, *The Equations of State of Solids at High Pressures and Temperatures* (Nauka, Moscow, 1968) [in Russian].
66. A. V. Bushman, G. I. Kanel', A. L. Ni, and V. E. Fortov, *Intense Dynamic Loading of Condensed Matter* (Taylor and Francis, London, 1993).
67. V. E. Fortov and I. V. Lomonosov, Phys. Usp. **57**, 219 (2014).
68. I. K. Krasyuk, P. P. Pashinin, A. Yu. Semenov, et al., Laser Phys. **26**, 094001 (2016).
69. V. Recoules, J. Clerouin, G. Zerah, et al., Phys. Rev. Lett. **96**, 055503 (2006).
70. N. A. Inogamov, V. V. Zhakhovsky, Yu. V. Petrov, et al., Contrib. Plasma Phys. **53**, 796 (2013).
71. P. R. Levashov, K. V. Khishchenko, I. V. Lomonosov, and V. E. Fortov, AIP Conf. Proc. **706**, 87 (2004).
72. K. V. Khishchenko, Tech. Phys. Lett. **30**, 829 (2004).
73. V. E. Fortov, V. V. Kim, I. V. Lomonosov, et al., Int. J. Impact Eng. **33**, 244 (2006).
74. N. A. Inogamov, S. I. Ashitkov, V. V. Zhakhovsky, et al., Appl. Phys. A **101**, 1 (2010).
75. N. A. Inogamov, V. V. Zhakhovsky, S. I. Ashitkov, et al., AIP Conf. Proc. **1278**, 590 (2010).
76. N. A. Inogamov, V. V. Zhakhovsky, S. I. Ashitkov, et al., Contrib. Plasma Phys. **51**, 367 (2011).
77. N. A. Inogamov, V. V. Zhakhovsky, S. I. Ashitkov, et al., J. Phys.: Conf. Ser. **500**, 112070 (2014).
78. N. A. Inogamov, V. V. Zhakhovskii, S. I. Ashitkov, et al., Appl. Surf. Sci. **255**, 9712 (2009).
79. N. A. Inogamov, A. Ya. Faenov, V. A. Khokhlov, et al., Contrib. Plasma Phys. **49**, 455 (2009).
80. N. A. Inogamov, V. V. Zhakhovsky, S. I. Ashitkov, et al., in *Proceedings of the International Symposium on High Power Laser Ablation, Santa Fe, NM, April 19–22, 2010,* p. 590.
81. L. V. Zhigilei, Z. Lin, and D. S. Ivanov, J. Phys. Chem. C **113**, 11892 (2009).
82. M. E. Povarnitsyn and T. E. Itina, Appl. Phys. A **117**, 175 (2014).
83. J. Hohlfeld, S.-S. Wellershoff, J. Guedde, et al., Chem. Phys. **251**, 237 (2000).
84. N. A. Inogamov, V. V. Zhakhovskii, and V. A. Khokhlov, J. Exp. Theor. Phys. **120**, 15 (2015).
85. Yu. V. Petrov, N. A. Inogamov, and K. P. Migdal, Izv. Kab.-Balk. Univ. **4** (3), 15 (2014).
86. N. A. Inogamov, V. V. Zhakhovsky, N. Hasegawa, et al., Appl. Phys. B **119**, 413 (2015).
87. V. A. Khokhlov, N. A. Inogamov, V. V. Zhakhovsky, et al., J. Phys.: Conf. Ser. **653**, 012003 (2015).
88. N. A. Inogamov, V. V. Zhakhovsky, V. A. Khokhlov, et al., Nanoscale Res. Lett. **11**, 177 (2016).
89. N. A. Inogamov, V. V. Zhakhovsky, and K. P. Migdal, Appl. Phys. A **122**, 432 (2016).
90. N. A. Inogamov and V. V. Zhakhovsky, J. Phys.: Conf. Ser. **681**, 012001 (2016).
91. A. Kuchmizhak, O. Vitrik, Yu. Kulchin, et al., Nanoscale **8**, 12352 (2016).
92. N. A. Inogamov, V. A. Khokhlov, Yu. V. Petrov, et al., AIP Conf. Proc. **1793**, 070012 (2017).
93. P. A. Danilov, D. A. Zayarnyi, S. I. Ionin, S. I. Kudryashov, A. A. Rudenko, A. A. Kuchmizhak, O. B. Vitrik, Yu. N. Kulchin, V. V. Zhakhovsky and N. A. Inogamov, JETP Lett. **104**, 759 (2016).
94. S. I. Anisimov, V. V. Zhakhovskii, N. A. Inogamov, S. A. Murzov, and V. A. Khokhlov, Quantum Electron. **47**, 509 (2017).
95. X. W. Wang, A. A. Kuchmizhak, X. Li, et al., Phys. Rev. Appl. **8**, 044016 (2017).
96. N. A. Inogamov, V. V. Zhakhovsky, and V. A. Khokhlov, J. Phys.: Conf. Ser. **946**, 012008 (2018).
97. V. V. Shepelev and N. A. Inogamov, J. Phys.: Conf. Ser. **946**, 012010 (2018).
98. A. Block, M. Liebel, R. Yu, et al., Sci. Adv. 5, eaav8965 (2019).
99. N. A. Inogamov, V. V. Zhakhovsky, V. A. Khokhlov, et al., J. Phys.: Conf. Ser. **774**, 012102 (2016).
100. N. A. Inogamov, S. I. Anisimov, Yu. V. Petrov, et al., Proc. SPIE **7005**, 70052F (2008).
101. N. A. Inogamov, Yu. V. Petrov, V. V. Zhakhovsky, et al., AIP Conf. Proc. **1464**, 593 (2012).
102. Yu. V. Petrov and N. A. Inogamov, JETP Lett. **98**, 278 (2013).
103. K. P. Migdal, Yu. V. Petrov, and N. A. Inogamov, Proc. SPIE **9065**, 906503 (2013).
104. N. A. Inogamov, V. V. Zhakhovsky, Yu. V. Petrov, et al., Proc. SPIE **9065**, 906502 (2013).
105. Yu. V. Petrov, N. A. Inogamov, and K. P. Migdal, in *Physics of Extreme States of Matter – 2013, JIHT*, Ed. by V. E. Fortov (2013), p. 33.
106. Yu. V. Petrov, N. A. Inogamov, S. I. Anisimov, et al., J. Phys.: Conf. Ser. **653**, 012087 (2015).
107. K. P. Migdal, Yu. V. Petrov, D. K. Il'nitsky, et al., Appl. Phys. A **122**, 408 (2016).
108. Yu. V. Petrov, N. A. Inogamov, A. V. Mokshin, and B. N. Galimzyanov, J. Phys.: Conf. Ser. **946**, 012096 (2018).
109. Yu. V. Petrov, N. A. Inogamov, K. P. Migdal, et al., J. Phys.: Conf. Ser. **1147**, 012069 (2019).
110. S. I. Anisimov and B. Rethfeld, Izv. Akad. Nauk, Ser. Fiz. **61**, 1642 (1997).
111. S. I. Anisimov and B. Rethfeld, Proc. SPIE **3093**, 192 (1997).
112. F. Ladstädter, U. Hohenester, P. Puschnig, and C. Ambrosch-Draxl, Phys. Rev. B **70**, 235125 (2004).
113. N. A. Inogamov, A. Ya. Faenov, V. V. Zhakhovsky, et al., Contrib. Plasma Phys. **51**, 419 (2011).
114. N. A. Inogamov, A. M. Oparin, Yu. V. Petrov, et al., JETP Lett. **69**, 310 (1999).

115. V. V. Zhakhovskii, K. Nishihara, S. I. Anisimov, and N. A. Inogamov, JETP Lett. **71**, 167 (2000).
116. N. A. Inogamov, V. V. Zhakhovskii, S. I. Ashitkov, Yu. V. Petrov, M. B. Agranat, S. I. Anisimov, K. Nishihara, and V. E. Fortov, J. Exp. Theor. Phys. **107**, 1 (2008).
117. S. I. Anisimov, N. A. Inogamov, A. M. Oparin, et al., Appl. Phys. A **69**, 617 (1999).
118. N. A. Inogamov, S. I. Anisimov, and B. Retfel'd, J. Exp. Theor. Phys. **88**, 1143 (1999).
119. E. Leveugle, D. S. Ivanov, and L. V. Zhigilei, Appl. Phys. A **79**, 1643 (2004).
120. M. E. Povarnitsyn, T. E. Itina, M. Sentis, et al., Phys. Rev. B **75**, 235414 (2007).
121. M. V. Shugaev, C. Wu, O. Armbruster, et al., MRS Bull. **41**, 12 (2016).
122. P. N. Mayer and A. E. Mayer, J. Appl. Phys. **124**, 035901 (2018).
123. S. I. Ashitkov, N. A. Inogamov, V. V. Zhakhovskii, Yu. N. Emirov, M. B. Agranat, I. I. Oleinik, S. I. Anisimov, and V. E. Fortov, JETP Lett. **95**, 176 (2012).
124. C. Wu, M. S. Christensen, J.-M. Savolainen, et al., Phys. Rev. B **91**, 035413 (2015).
125. K. Sokolowski-Tinten, J. Bialkowski, A. Cavalleri, et al., Phys. Rev. Lett. **81**, 224 (1998).
126. A. Ya. Faenov, N. A. Inogamov, V. V. Zhakhovskii, et al., Appl. Phys. Lett. **94**, 231107 (2009).
127. N. A. Inogamov, V. V. Zhakhovsky, A. Y. Faenov, et al., Appl. Phys. A **101**, 87 (2010).
128. M. Ishino, A. Ya. Faenov, M. Tanaka, et al., J. Appl. Phys. **109**, 013504 (2011).
129. N. A. Inogamov, A. Ya. Faenov, V. V. Zhakhovskii, et al., Contrib. Plasma Phys. **51**, 361 (2011).
130. Y. Cherednikov, N. A. Inogamov, and H. M. Urbassek, J. Opt. Soc. Am. B **28**, 1817 (2011).
131. N. A. Inogamov, S. I. Anisimov, V. V. Zhakhovskii, et al., Opt. Zh. **78**, 5 (2011).
132. M. Ishino, A. Faenov, M. Tanaka, et al., AIP Conf. Proc. **1465**, 236 (2012).
133. Y. Cherednikov, N. A. Inogamov, and H. M. Urbassek, Phys. Rev. B **88**, 134109 (2013).
134. M. Ishino, A. Faenov, M. Tanaka, et al., Proc. SPIE **8849**, 88490F (2013).
135. M. Ishino, N. Hasegawa, M. Nishikino, et al., J. Appl. Phys. **116**, 183302 (2014).
136. M. Ishino, N. Hasegawa, M. Nishikino, et al., Proc. SPIE **9598**, 958904 (2015).
137. T. A. Pikuz, A. Ya. Faenov, N. Ozaki, et al., J. Appl. Phys. **120**, 035901 (2016).
138. N. A. Inogamov, V. A. Khokhlov, V. V. Zhakhovsky, and Yu. V. Petrov, J. Phys.: Conf. Ser. **946**, 012009 (2018).
139. Y. Kohmura, V. Zhakhovsky, D. Takei, et al., Appl. Phys. Lett. **112**, 123103 (2018).
140. S. Yu. Grigoryev, B. V. Lakatosh, M. S. Krivokorytov, et al., Phys. Rev. Appl. **10**, 064009 (2018).
141. S. Yu. Grigoryev, S. A. Dyachkov, V. A. Khokhlov, et al., J. Phys.: Conf. Ser. **1147**, 012067 (2019).
142. A. Ya. Vorobyev and C. Guo, Opt. Express **14**, 2164 (2006).
143. A. Ya. Vorobyev and C. Guo, Appl. Phys. Lett. **92**, 041914 (2008).
144. R. N. Patel, T. Schröder, N. Wan, et al., Light: Sci. Appl. **5**, e16032 (2016).
145. E. L. Gurevich, Phys. Rev. E **83**, 031604 (2011).
146. A. A. Ionin, S. I. Kudryashov, S. V. Makarov, et al., Laser Phys. Lett. **13**, 025603 (2015).
147. V. V. Zhakhovskii, N. A. Inogamov, and K. Nishihara, JETP Lett. **87**, 423 (2008).
148. V. V. Zhakhovskii, N. A. Inogamov, and K. Nishihara, J. Phys.: Conf. Ser. **112**, 042080 (2008).
149. Yu. V. Petrov, V. V. Zhakhovskii, N. A. Inogamov, et al., Proc. SPIE **7005**, 70051W (2008).
150. N. A. Inogamov, V. V. Zhakhovsky, S. I. Ashitkov, et al., Eng. Failure Anal. **47**, 328 (2015).
151. S. I. Ashitkov, P. S. Komarov, A. V. Ovchinnikov, E. V. Struleva, V. V. Zhakhovsky, N. A. Inogamov, and M. B. Agranat, Quantum Electron. **44**, 535 (2014).
152. N. A. Inogamov, V. V. Zhakhovsky, V. A. Khokhlov, et al., J. Phys.: Conf. Ser. **510**, 012041 (2014).
153. S. I. Ashitkov, S. A. Romashevskii, P. S. Komarov, A. A. Burmistrov, V. V. Zhakhovsky, N. A. Inogamov, and M. B. Agranat, Quantum Electron. **45**, 547 (2015).
154. Yu. V. Petrov, N. A. Inogamov, V. V. Zhakhovsky, and V. A. Khokhlov, Contrib. Plasma Phys., **59**, 419 (2019); arXiv:1812.09929 [physics.comp-ph].
155. S. I. Anisimov, N. M. Kuznetsov, and E. F. Nogotov, Teplofiz. Vys. Temp. **2**, 337 (1964).
156. S. I. Anisimov, Sov. Tech. Phys. **9**, 480 (1964).
157. S. I. Anisimov and V. I. Matsaev, Preprint PLF-14 (Max-Planck Inst. Plasma Phys., Garching, 1979).
158. S. I. Anisimov, V. V. Zhakhovskii, and K. Nishihara, in *Proceedings of the 13th International Conference on Laser Interaction and Related Plasma Phenomena, Monterey, CA, 1997*, p. 56.
159. V. V. Zhakhovskii, K. Nishihara, and S. I. Anisimov, JETP Lett. **66**, 99 (1997).
160. S. I. Anisimov, V. V. Zhakhovskii, and V. E. Fortov, JETP Lett. **65**, 755 (1997).
161. V. V. Zhakhovskii, S. V. Zybin, K. Nishihara, and S. I. Anisimov, Phys. Rev. Lett. **83**, 1175 (1999).
162. S. I. Anisimov and Yu. V. Khodyko, Sov. Tech. Phys. **8**, 993 (1963).
163. S. I. Anisimov and V. I. Fisher, in *Proceedings of the IUTAM Symposium on Dynamics of Ionized Gases, Tokyo, 1971*, p. 38.
164. S. I. Anisimov and V. I. Fisher, Sov. Tech. Phys. **16**, 2041 (1971).
165. S. I. Anisimov, M. F. Ivanov, P. P. Pashinin, and A. M. Prokhorov, JETP Lett. **22**, 161 (1975).
166. S. I. Anisimov and Yu. V. Medvedev, Sov. Tech. Phys. **33**, 1123 (1988).
167. S. I. Anisimov, Sov. Tech. Phys. **5**, 1057 (1960).
168. C. I. Anisimov and N. M. Kuznetsov, Prikl. Mekh. Tekh. Fiz., No. 6, 167 (1961).
169. B. S. Luk'yanchuk and S. I. Anisimov, Proc. SPIE **5448**, 95 (2004).

170. S. I. Anisimov and V. A. Kravchenko, Z. Naturforsch. A **40**, 8 (1985).

171. S. A. Lifits, S. I. Anisimov, and J. Meyer ter Vehn, Z. Naturforsch. A **47**, 453 (1992).

172. S. I. Anisimov, A. M. Prokhorov, and V. E. Fortov, Izv. Akad. Nauk SSSR, Ser. Fiz. **46**, 1081 (1982).

173. B. Albertazzi, N. Ozaki, V. Zhakhovsky, et al., Sci. Adv. **3**, e160270 (2017).

174. S. I. Anisimov, A. V. Konyukhov, A. P. Likhachev, et al., in *Mathematical Simulation, Collection of Articles*, Ed. by O. M. Belotserkovskii V. A. Gushchin (Nauka, Moscow, 2003) [in Russian].

175. A. V. Konyukhov, A. P. Likhachev, A. M. Oparin, S. I. Anisimov, and V. E. Fortov, J. Exp. Theor. Phys. **98**, 811 (2004).

176. A. V. Konyukhov, A. P. Likhachev, V. E. Fortov, A. M. Oparin, and S. I. Anisimov, J. Exp. Theor. Phys. **104**, 670 (2007).

177. A. P. Likhachev, A. V. Konyukhov, V. E. Fortov, et al., AIP Conf. Proc. **1195**, 37 (2009).

178. A. V. Konyukhov, A. P. Likhachev, V. E. Fortov, K. V. Khishchenko, S. I. Anisimov, A. M. Oparin, and I. V. Lomonosov, JETP Lett. **90**, 18 (2009).

179. A. V. Konyukhov, A. P. Likhachev, V. E. Fortov, S. I. Anisimov, and A. M. Oparin, JETP Lett. **90**, 25 (2009).

180. A. Konyukhov, A. Likhachev, V. Fortov, and S. Anisimov, in *Proceedings of the 28th International Symposium on Shock Waves*, Ed. by K. Kontis (Springer, Berlin, 2012), Vol. 2, p. 531.

181. S. I. Anisimov and Ya. B. Zel'dovich, Sov. Tech. Phys. Lett. **3**, 445 (1977).

182. S. I. Anisimov, Ya. B. Zel'dovich, N. A. Inogamov, and M. F. Ivanov, Prog. Astronaut. Aeronaut. **87**, 218 (1983).

183. S. I. Anisimov, A. M. Prokhorov, P. P. Pashinin, et al., Sov. Tech. Phys. Lett. **4**, 157 (1978).

184. M. B. Agranat, S. I. Anisimov, S. I. Ashitkov, V. V. Zhakhovskii, N. A. Inogamov, P. S. Komarov, A. V. Ovchinnikov, V. E. Fortov, V. A. Khokhlov, and V. V. Shepelev, JETP Lett. **91**, 471 (2010).

185. V. V. Zhakhovskii and N. A. Inogamov, JETP Lett. **92**, 521 (2010).

186. N. A. Inogamov, V. V. Zhakhovskii, V. A. Khokhlov, and V. V. Shepelev, JETP Lett. **93**, 226 (2011).

187. V. V. Zhakhovsky, M. M. Budzevich, N. A. Inogamov, et al., Phys. Rev. Lett. **107**, 135502 (2011).

188. B. J. Demaske, V. V. Zhakhovsky, N. A. Inogamov, et al., AIP Conf. Proc. **1426**, 1163 (2012).

189. B. J. Demaske, V. V. Zhakhovsky, N. A. Inogamov, et al., AIP Conf. Proc. **1426**, 1303 (2012).

190. B. J. Demaske, V. V. Zhakhovsky, N. A. Inogamov, and I. I. Oleynik, Phys. Rev. B **87**, 054109 (2013).

191. V. A. Khokhlov, N. A. Inogamov, V. V. Zhakhovsky, and S. I. Anisimov, in *Physics of Extreme States of Matter – 2013*, Ed. by V. E. Fortov (JIHT, Moscow, 2013), p. 61.

192. R. Perriot, V. V. Zhakhovsky, N. A. Inogamov, and I. I. Oleynik, J. Phys.: Conf. Ser. **500**, 172008 (2014).

193. V. V. Zhakhovsky, N. A. Inogamov, B. J. Demaske, et al., J. Phys.: Conf. Ser. **500**, 172007 (2014).

194. S. I. Ashitkov, V. V. Zhakhovsky, N. A. Inogamov, et al., AIP Conf. Proc. **1793**, 100035 (2017).

195. V. V. Zhakhovsky, K. P. Migdal, N. A. Inogamov, and S. I. Anisimov, AIP Conf. Proc. **1793**, 070003 (2017).

196. V. V. Zhakhovsky, B. J. Demaske, N. A. Inogamov, et al., AIP Conf. Proc. **1464**, 102 (2012).

197. V. V. Zhakhovsky, M. M. Budzevich, N. A. Inogamov, et al., AIP Conf. Proc. **1426**, 1227 (2012).

198. D. K. Ilnitsky, V. A. Khokhlov, N. A. Inogamov, et al., J. Phys.: Conf. Ser. **500**, 032021 (2014).

199. S. I. Anisimov, M. B. Agranat, S. I. Ashitkov, et al., Sov. Phys. Solid State **29**, 1875 (1987).

200. M. B. Agranat, S. I. Anisimov, S. I. Ashitkov, et al., JETP Lett. **66**, 699 (1997).

201. M. B. Agranat, S. I. Anisimov, S. I. Ashitkov, et al., JETP Lett. **67**, 953 (1998).

202. M. B. Agranat, S. I. Anisimov, S. I. Ashitkov, et al., J. Exp. Theor. Phys. **86**, 1184 (1998).

203. M. B. Agranat, S. I. Anisimov, S. I. Ashitkov, et al., J. Exp. Theor. Phys. **88**, 370 (1999).

204. B. Retfel'd, V. V. Temnov, K. Sokolovski-Tinten, et al., J. Opt. Technol. **71**, 348 (2004).

205. M. B. Agranat, S. I. Anisimov, S. I. Ashitkov, A. V. Ovchinnikov, P. S. Kondratenko, D. S. Sitnikov, and V. E. Fortov, JETP Lett. **83**, 501 (2006).

206. M. B. Agranat, S. I. Anisimov, S. I. Ashitkov, et al., Appl. Surf. Sci. **253**, 6276 (2007).

207. M. B. Agranat, S. I. Anisimov, S. I. Ashitkov, et al., Proc. SPIE **6720**, 672002 (2007).

208. S. I. Anisimov, N. A. Inogamov, Yu. V. Petrov, et al., Appl. Phys. A **92**, 797 (2008).

209. S. I. Anisimov, N. A. Inogamov, Yu. V. Petrov, et al., Appl. Phys. A **92**, 939 (2008).

210. V. V. Zhakhovskii, N. A. Inogamov, Yu. V. Petrov, et al., Appl. Surf. Sci. **255**, 9592 (2009).

211. S. I. Ashitkov, M. B. Agranat, G. I. Kanel', P. S. Komarov, and V. E. Fortov, JETP Lett. **92**, 516 (2010).

212. N. A. Inogamov, S. I. Anisimov, V. V. Zhakhovsky, et al., Proc. SPIE **7996**, 79960T (2010).

213. S. I. Ashitkov, N. A. Inogamov, P. S. Komarov, et al., AIP Conf. Proc. **1464**, 120 (2012).

214. M. B. Agranat, S. I. Ashitkov, A. V. Ovchinnikov, D. S. Sitnikov, A. A. Yurkevich, O. V. Chefonov, L. T. Perel'man, S. I. Anisimov, and V. E. Fortov, JETP Lett. **101**, 598 (2015).

215. S. I. Ashitkov, P. S. Komarov, V. V. Zhakhovsky, et al., J. Phys.: Conf. Ser. **774**, 012097 (2016).

216. S. I. Ashitkov, P. S. Komarov, E. V. Struleva, et al., J. Phys.: Conf. Ser. **946**, 012002 (2018).

217. S. I. Ashitkov, P. S. Komarov, M. B. Agranat, G. I. Kanel, and V. E. Fortov, JETP Lett. **98**, 384 (2013).

218. G. I. Kanel', S. V. Razorenov, G. V. Garkushin, S. I. Ashitkov, P. S. Komarov, and M. B. Agranat, Phys. Solid State **56**, 1569 (2014).

219. S. I. Ashitkov, P. S. Komarov, E. V. Struleva, M. B. Agranat, and G. I. Kanel, JETP Lett. **101**, 276 (2015).

220. G. I. Kanel', E. B. Zaretskii, S. V. Razorenov, S. I. Ashitkov, and V. E. Fortov, Phys. Usp. **60**, 490 (2017).
221. N. A. Inogamov, Sov. Tech. Phys. Lett. **10**, 323 (1984).
222. R. Z. Sagdeev, S. I. Anisimov, S. B. Zhitenev, et al., Sov. Phys. Dokl. **29**, 958 (1984).
223. N. A. Inogamov, Sov. Phys. Dokl. **29**, 660 (1984).
224. S. B. Zhitenev, N. A. Inogamov, and A. B. Konstantinov, Inzh.-Fiz. Zh. **50**, 751 (1986).
225. J. Kissel, R. Z. Sagdeev, J. L. Bertaux, et al., Nature (London, U.K.) **321**, 280 (1986).
226. N. A. Inogamov, Inzh.-Fiz. Zh. **52**, 553 (1987).
227. R. Z. Sagdeev, J. Kissel, E. N. Evlanov, et al., Astron. Astrophys. **187**, 179 (1987).
228. S. I. Anisimov, S. B. Zhitenev, N. A. Inogamov, and A. B. Konstantinov, Sov. Tech. Phys. Lett. **17**, 179 (1991).
229. N. A. Inogamov, A. B. Konstantinov, S. I. Anisimov, and S. B. Zhitenev, Sov. Phys. JETP **72**, 948 (1991).
230. N. A. Inogamov and R. A. Syunyaev, Astron. Lett. **25**, 269 (1999).
231. N. A. Inogamov and R. A. Syunyaev, Astron. Lett. **29**, 791 (2003).
232. N. A. Inogamov and R. A. Syunyaev, Astron. Lett. **36**, 848 (2010).
233. N. A. Inogamov and R. A. Syunyaev, Astron. Lett. **36**, 835 (2010).
234. N. A. Inogamov and R. A. Syunyaev, Astron. Lett. **41**, 693 (2015).
235. N. I. Shakura and R. A. Sunyaev, Astron. Astrophys. **500**, 33 (1973).
236. R. Popham and R. Sunyaev, Astrophys. J. **547**, 355 (2001).
237. M. A. Belyaev, R. R. Rafikov, and J. M. Stone, Astrophys. J. **770**, 67 (2013).
238. N. A. Inogamov and V. V. Zhakhovskii, JETP Lett. **100**, 4 (2014).
239. V. A. Khokhlov, V. V. Zhakhovsky, K. V. Khishchenko, et al., J. Phys.: Conf. Ser. **774**, 012100 (2016).
240. V. A. Khokhlov, N. A. Inogamov, V. V. Zhakhovsky, et al., AIP Conf. Proc. **1793**, 100038 (2017).
241. N. A. Inogamov and V. V. Zhakhovsky, Lobachevskii J. Math. **38**, 914 (2017).
242. V. V. Shepelev, N. A. Inogamov, S. V. Fortova, et al., J. Phys.: Conf. Ser. **1128**, 012092 (2018).
243. N. A. Inogamov, V. V. Zhakhovsky, and V. A. Khokhlov, AIP Conf. Proc. **1979**, 190002 (2018).
244. J. M. Liu, Opt. Lett. **7**, 196 (1982).
245. D. Wortmann, J. Koch, M. Reininghaus, et al., J. Laser Appl. **24**, 042017 (2012).
246. C. Unger, J. Koch, L. Overmeyer, and B. N. Chichkov, Opt. Express **20**, 24864 (2012).
247. F. Korte, J. Koch, and B. N. Chichkov, Appl. Phys. A **79**, 879 (2004).
248. A. I. Ignatov, V. V. Zhakhovsky, A. M. Merzlikin, and N. A. Inogamov, J. Phys.: Conf. Ser. **1092**, 012051 (2018).
249. A. I. Ignatov, V. V. Zhakhovsky, A. M. Merzlikin, and N. A. Inogamov, J. Phys.: Conf. Ser. **1092**, 012052 (2018).
250. N. Inogamov, V. Zhakhovsky, and V. Khokhlov, AIP Conf. Proc. **1979**, 190001 (2018).
251. N. Inogamov, V. Zhakhovsky, and V. Khokhlov, arXiv:1803.07343v1 (2018).
252. N. A. Inogamov, V. A. Khokhlov, and V. V. Zhakhovsky, JETP Lett. **108**, 439 (2018).
253. V. A. Khokhlov, N. A. Inogamov, V. V. Zhakhovsky, and Yu. V. Petrov, arXiv: 1811.11990 [cond-mat.meshall] (2018).
254. Yu. V. Petrov, V. A. Khokhlov, V. V. Zhakhovsky, and N. A. Inogamov, arXiv: 1812.09109 [physics.compph] (2018).
255. S. A. Dyachkov, V. V. Zhakhovsky, A. N. Parshikov, and N. A. Inogamov, J. Phys.: Conf. Ser. **1147**, 012064 (2019).
256. M. S. Egorova, S. A. Dyachkov, A. N. Parshikov, and V. V. Zhakhovsky, Comput. Phys. Comm. **234**, 112 (2019).

Translated by V. Astakhov